

# On constraining the mesoscale eddy energy dissipation time-scale

J. Mak<sup>1,2</sup>, A. Avdis<sup>3,4</sup>, T. W. David<sup>5</sup>, H. S. Lee<sup>1</sup>, Y. Na<sup>1</sup>, Y. Wang<sup>1,2</sup> and F. E. Yan<sup>1</sup>

<sup>1</sup>Department of Ocean Science, Hong Kong University of Science and Technology

<sup>2</sup>Center for Ocean Research in Hong Kong and Macau, Hong Kong University of Science and Technology

<sup>3</sup>Department of Earth Science and Engineering, Imperial College London

<sup>4</sup>HPC department, Boston Limited

<sup>5</sup>Laboratoire de Physique, École Normale Supérieure de Lyon

## Key Points:

- Constraining the mesoscale eddy energy dissipation time-scale in the ocean via a simple and computationally inexpensive inverse calculation
- Shortest dissipation time-scale in Southern Ocean, Western Boundary Currents, and ocean western boundaries
- Computes a spatially varying lower bound dissipation time-scale to guide future investigations

arXiv:2208.07634v1 [physics.ao-ph] 16 Aug 2022

---

Corresponding author: Julian Mak, [julian.c.l.mak@gmail.com](mailto:julian.c.l.mak@gmail.com)

**Abstract**

A physically plausible lower bound on the spatially varying geostrophic mesoscale eddy energy dissipation time-scale within the ocean, related to the geographical energy transfer rate out of the geostrophic mesoscales, is provided by means of a simple and computational inexpensive inverse calculation. Data diagnosed from a high resolution global configuration ocean simulation is supplied to a parameterized model of the geostrophic mesoscale eddy energy, from which the dissipation time-scale results as a solution to an optimization calculation. We find that the dissipation time-scale is shortest in the Southern Ocean, in the Western Boundary Currents, and on the western boundaries, consistent with the expectation that these regions are notable sites of baroclinic activity with processes leading to energy transfer out of the geostrophic mesoscales. Although our solution should be interpreted as a lower bound given the assumptions going into the calculation, it serves as an important physically consistent base line reference for further investigations into ocean energetics, as well as for an intended inference calculation that is more complete but also much more complex.

**Plain Language Summary**

Energy plays an important role in quantifying the magnitude of motions at different time and spatial scales. Many different dynamical processes contribute to energy transfers within the ocean, and constraining the rate of transfer remains a formidable challenge. This work provides a leading-order constraint on the overall magnitude and spatial distribution of an eddy energy dissipation time-scale, which relates to the rate of energy transfer out of the motions at 10 to 100 km in the ocean, where rotation and stratification play a leading order role in the dynamics. A time-scale is “backed out” from a model via an inverse approach: given a model for the eddy energy evolution and what we should end up with (the eddy energy signature), what should we have started off with in the first place (the dissipation time-scale)? Although our solution should be interpreted as a lower bound given the assumptions going into the calculation, it serves as an important physically consistent base line reference for further investigations into ocean energetics, as well as for an intended inference calculation that is more complete but also much more complex.

**1 Introduction**

The ocean, being a key component of the Earth system, plays a central role in the Earth’s energy and biogeochemical cycles through its ability to store and transport large amounts of tracers (e.g., Zhang & Vallis, 2013; Adkins, 2013; Ferrari et al., 2014; Burke et al., 2015; Bopp et al., 2017; Jansen, 2017; Takano et al., 2018; Galbraith & de Lavergne, 2019). A key component is the transport provided by the ocean circulation, taken here to mean both the large-scale mean circulation, as well as the smaller-scale eddy motions. The large-scale mean motions tend to generate smaller-scale eddy motions via instabilities, but the smaller-scale eddy motions also interact and feedback onto the large-scale mean. The ability to represent the multi-scale interaction faithfully (via explicit or sub-grid modeling means), besides the theoretical interest, is of central importance to ocean model performance, which impacts our ability to predict and assess impacts within the ocean component as well as the wider Earth system (e.g. Hewitt et al., 2017; Fox-Kemper et al., 2019).

An important quantity relating to dynamics at the relevant space and/or time-scales is the energy, and there has been ongoing theoretical, numerical and observational research into quantifying and constraining ocean energy content and pathways. Ferrari and Wunsch (2009, 2010) provide one of the more recent reviews of the global energy content and pathways of the overall ocean energetic cycles, though the authors note that there are still relatively large uncertainties associated with the magnitudes

as well as spatial distributions in the energy fluxes. From an ocean modeling point of view, energetically constrained parameterizations have been increasingly proposed and investigated, and such parameterizations have led to model improvements (e.g. Gaspar et al., 1990; Cessi, 2008; Eden & Greatbatch, 2008; D. P. Marshall & Adcroft, 2010; D. P. Marshall et al., 2012; Olbers & Eden, 2013; Eden et al., 2014; Jansen & Held, 2014; Mak et al., 2018; Nielsen et al., 2018; Bachman, 2019; Jansen et al., 2019; Mak et al., 2022). Beyond improving our understanding of the dynamics within the ocean, constraints for the energy pathways play an important role in limiting the magnitude and form of energy transfers between different dynamical components, which is also expected to lead to improved performance of numerical ocean models via improvements to sub-grid parameterizations of dynamical processes.

The focus of the present work is on providing a leading order constraint on the energy pathway associated with the ocean geostrophic mesoscales, where the dynamics are strongly constrained by rotation and stratification. Analogous to processes such as internal waves where the impact of energy supply and removal will affect quantities such as diapycnal mixing, the energy content and pathways in the geostrophic mesoscale is expected to impact eddy induced advection and isoneutral diffusion, usually quantified by an eddy induced velocity coefficient or the Gent–McWilliams coefficient (Gent & McWilliams, 1990; Gent et al., 1995) and an isoneutral diffusion coefficient (Redi, 1982; Griffies, 1998), respectively. Eddy energy content and removal rates will affect the associated eddy–mean-flow feedbacks, with consequences for the global overturning circulation and stratification profile. Such an influence was demonstrated, for example, in the work of Mak et al. (2022) for prognostic calculations within a global ocean circulation model via an eddy energy constrained mesoscale eddy parameterization scheme (GEOMETRIC; D. P. Marshall et al., 2012; Mak et al., 2018). In that work, the model global ocean circulation and stratification were found to be acutely sensitive to modest changes in an eddy energy dissipation time-scale  $\lambda^{-1}$ , and were comparable sensitivities with respect to significant variations (halving and doubling) in the Southern Ocean wind forcing magnitude. While we do not expect such significant changes in the Southern Ocean wind forcing (e.g. Lin et al., 2018), analogous constraints for the eddy energy dissipation time-scale, related in turn to the eddy energy flux out of the geostrophic mesoscales, are lacking.

While the transfer of energy into the mesoscale is known to be primarily via baroclinic instability, accessing the available potential energy at the large planetary scales arising from large-scale wind and thermodynamic forcing (Ferrari & Wunsch, 2009, 2010), there are many dynamical processes that can lead to energy fluxes out of the mesoscale. These include but are not limited to: direct return to the mean flow, via an inverse cascade in rotationally dominant quasi-two-dimensional systems (e.g. Salmon, 1980; Jansen et al., 2019; Bachman, 2019); relative wind stress effects, whereby the atmospheric wind forcing can spindown baroclinic eddies (e.g. Zhai et al., 2012; Xu et al., 2016; Rai et al., 2021); bottom drag (e.g. Sen et al., 2008); non-propagating form drag arising from bathymetric form stress (e.g. Klymak, 2018; Klymak et al., 2021); scattering into lee waves by geostrophic flow interaction with the bottom topography (e.g. Nikurashin & Ferrari, 2011; Nikurashin et al., 2013; Melet et al., 2014, 2015; L. Yang et al., 2018, 2021); loss of balance, from secondary fluid instabilities of the mesoscale eddy motions themselves (e.g. Molemaker et al., 2005; Barkan et al., 2017; Rocha et al., 2018; Chouksey et al., 2018). While there are suggestions that some processes are more efficient at transferring energy out of the mesoscale (e.g., non-propagating form drag; Klymak et al., 2021), an overall quantification on the geographical distribution of the energy transfer rate is absent.

Given the preceding discussion, we are primarily interested in providing an overall estimate for the spatial distribution of the eddy energy dissipation time-scale  $\lambda^{-1}$ , to serve as a leading order constraint for (1) the energy fluxes out of the geostrophic

mesoscales, (2) the various dynamical components leading to the aforementioned energy flux, (3) the development of further parameterizations of the energy fluxes, and (4) further theoretical, numerical and observation works into the ocean energetic cycles. In this work, we perform an inference calculation for a spatially varying  $\lambda^{-1}$  via an inverse approach, and illustrate the approach via the GEOMETRIC description for the geostrophic mesoscale eddy energy evolution (although other choices are possible, e.g. MEKE from Jansen et al., 2019). Such inference calculations have a beneficial side effect of providing a way to tune for uncertain parameters for use in prognostic numerical models.

As will be detailed and argued later, while one would ideally like to carry out a *dynamically* constrained inference calculation, the associated calculation is numerically complex and computationally intensive (e.g. requiring derivation of adjoint models given the expected large amount of degrees of freedom to maintain computational feasibility; Wunsch, 1996; Kalnay, 2002; Gunzburger, 2003). As a precursor to the proposed difficult but more complete dynamically constrained inference calculation, we report here a kinematic/diagnostic-type inference calculation that is much simpler and computationally inexpensive, with the caveat that there are simplifying assumptions involved, resulting in a spatially varying  $\lambda^{-1}$  that will be argued to be a physically plausible *lower bound*. In that sense, the present work reports a calculation that can serve as a prior the proposed dynamically constrained inference calculation. Additionally, the present work provides some exposure to the methodology and associated computational tools that are perhaps less well-known in the field of earth system science.

In §2 we provide details to the mesoscale version of the GEOMETRIC parameterization, an overview of the inference and inverse approach, and the implementation details of the diagnostic-type inference problem for the geostrophic mesoscale eddy energy dissipation time-scale  $\lambda^{-1}$ . Analyses of the characteristics of the resulting solutions are detailed in §3. In §4 we investigate the consequences of utilizing the inferred solution in a prognostic model, providing some support that the reported dissipation time-scale is a physically plausible lower bound. In §5 we provide outlooks on the proposed dynamically constrained inference calculation to improve our understanding of ocean energy pathways, parameterization of energy pathways, and for inferring uncertain system parameters.

## 2 Methodology and implementation

### 2.1 GEOMETRIC

For this work, we consider the GEOMETRIC description (D. P. Marshall et al., 2012) as a model for the evolution of mesoscale eddy energy. The choice of GEOMETRIC is made for its theoretical foundations (D. P. Marshall et al., 2012; Maddison & Marshall, 2013) and its demonstrated capabilities in recovering some key ocean sensitivities possessed by high resolution numerical models that permit and/or resolve mesoscale eddies in prognostic coarse resolution models (Mak et al., 2018, 2022); however we stress again that other choices such as MEKE from Jansen et al. (2019) would be possible with suitable adaptations of the methodology detailed below. Denoting  $\hat{E} = \int E dz$  as the depth-integrated total eddy energy, the mesoscale version of GEOMETRIC suggests we take (cf. Eq. 1 of Mak et al., 2022)

$$\kappa_{\text{gm}} = \alpha \frac{\hat{E}}{\int M^2/N dz}, \quad (1)$$

where  $\kappa_{\text{gm}}$  is the eddy induced velocity coefficient (c.f. Gent & McWilliams, 1990; Gent et al., 1995),  $\alpha$  is a non-dimensional tuning parameter, and  $M^2 = |\nabla_H b|$  and  $N^2 = \partial b/\partial z$  are the mean horizontal and vertical buoyancy gradients respectively. In

a prognostic calculation,  $\hat{E}$  evolves according to the parameterized eddy energy budget (cf. Eq. 2 of Mak et al., 2022)

$$\frac{d\hat{E}}{dt} + \underbrace{\nabla_H \cdot \left( (\tilde{\mathbf{u}}^z - |c| \mathbf{e}_x) \hat{E} \right)}_{\text{advection}} = \underbrace{\int \kappa_{\text{gm}} \frac{M^4}{N^2} dz}_{\text{source}} - \underbrace{\lambda \hat{E}}_{\text{dissipation}} + \underbrace{\eta_E \nabla_H^2 \hat{E}}_{\text{diffusion}}, \quad (2)$$

where  $\tilde{\mathbf{u}}^z$  is the depth-averaged mean flow,  $|c|$  is the long Rossby wave phase speed,  $\lambda$  is a linear eddy energy dissipation rate (so that  $\lambda^{-1}$  is the eddy energy dissipation time-scale of principal focus in this work), and  $\eta_E$  is an eddy energy diffusion coefficient. From prognostic calculations in Mak et al. (2022), the dominant contributions in Eq. (2) were found to be from the source and dissipation, with secondary contributions from diffusion and advection, though the latter two terms are important for the resulting eddy energy spatial distribution.

The principal aim of this work will be on constraining the spatial distribution of  $\lambda^{-1}(\phi, \theta)$  (where  $\phi$  and  $\theta$  denote the longitude and latitude respectively), here taken to encapsulate all the aforementioned dynamical processes that leads to an energy flux out of the mesoscale. This is of course a rather drastic approximation, although there is some suggestion that a dominant source of eddy energy removal from the mesoscale could be from non-propagating form drag (Klymak, 2018; Klymak et al., 2021), and the energy transfer arising from non-propagating form drag is better represented as a linear drag and expected to largely depend on the bathymetry. We also make the simplifying assumptions of taking both  $\eta_E$  and  $\alpha$  to be a prescribed constant. For  $\eta_E$ , this is partially justified *a priori*, where we expect the diffusion term to be of secondary importance in the evolution of the parameterized eddy energy in prognostic calculations, and *a posteriori*, where the inferred solutions were found not to be overly sensitive to the choice of  $\eta_E$ . For  $\alpha$ , this is mainly for simplicity, and it is known  $\alpha$  does vary in space (Poulsen et al., 2019). The inferred solution will be seen to display some sensitivity to the value of  $\alpha$  through its role in the source term. The possibility of a joint inference calculation for  $\lambda^{-1}$  and  $\alpha$  are discussed in §5.

## 2.2 Parameter inference problem

The inference calculation for  $\lambda^{-1}(\phi, \theta)$  here utilizes the variational approach (e.g. Kalnay, 2002). In the general case, we have state variables  $\mathbf{w}$  that depend on control variable  $\lambda^{-1}(\phi, \theta)$  via some model  $F(\mathbf{w}; \lambda^{-1}) = 0$ , and the aim is to seek  $\lambda^{-1}(\phi, \theta)$  such that the mismatch between some target data  $\mathbf{w}_{\text{data}}$  and  $\mathbf{w}$  is minimized, possibly subject to some regularization  $\mathcal{R}(\mathbf{w}; \lambda)$  that encapsulates our prior expectations for the state and/or control variables. A variational approach is for example utilized in the Estimating the Circulation and Climate of the Ocean framework (ECCO; e.g. Forget et al., 2015; Fukumori et al., 2018): the ocean state variables (e.g. temperature, salinity) are the state variables in ECCO, and the ECCO framework seeks to adjust the control variables (e.g. wind forcing, initial ocean state, parameterization parameters) with the aim to minimize the mismatch to observational data (e.g. sea surface height, hydrographic sections, currents strengths) over time, subject to regularizations (e.g. the wind forcing not deviating too far from climatology) and the constraint that the calculated state satisfies the dynamical equations as implemented in MITgcm (J. Marshall, Adcroft, et al., 1997; J. Marshall, Hill, et al., 1997). Within ECCO, the optimization problem is achieved through an adjoint method (e.g., Wunsch, 1996; Kalnay, 2002; Gunzburger, 2003).

Ultimately the aim would be to carry out a dynamically constrained inference problem, where the parameterized eddy energy equation Eq. (2) would be coupled to an ocean global general circulation model, so that the evolution of the parameterized eddy energy profile is dynamically and self-consistently interacting with the evolving the ocean state (e.g.  $M^2$ ,  $N^2$ ,  $\tilde{\mathbf{u}}^z$  and  $|c|$  etc.), and infer for the spatially varying  $\lambda^{-1}(\phi, \theta)$

or other choices of control variables. Such an inference calculation could leverage the ECCO framework with appropriate modifications of the constraining equations. However, such an endeavor will require a significant investment in human development time and computational resources, exacerbated by the fact that we have no leading order constraints of  $\lambda^{-1}(\phi, \theta)$  to serve as a prior for regularizing the inverse problem. Thus, with the dynamically constrained inference as the eventual goal, in this work we present a useful complementary calculation that serves to provide a first leading order estimate for  $\lambda^{-1}(\phi, \theta)$ . We note that we can in principle diagnose the mean state variables required for the eddy energy equation Eq. (2) from a high resolution global circulation model, and supply the inference calculation with prescribed physical state variables. The result is that we substantially reduce the complexity of the constraining model  $F(\mathbf{w}; \lambda^{-1}) = 0$ , since we no longer need the calculation to be coupled to a dynamical model. A drawback however is that dynamical feedbacks are removed; and consequences are discussed at the end of the present subsection.

With sufficiently long time-averaging and with the assumption that the evolution of the eddy energy has reached a statistically steady state, the constraining model becomes an elliptic problem given by

$$F(\hat{E}; \lambda^{-1}) \equiv \underbrace{\eta_E \nabla_H^2 \hat{E}}_{\text{diffusion}} - \underbrace{\lambda \hat{E}}_{\text{dissipation}} + \underbrace{\alpha \frac{\int M^4/N^2 dz}{\int M^2/N dz} \hat{E}}_{\text{source}} - \underbrace{\nabla_H \cdot ((\tilde{\mathbf{u}}^z - |c| \mathbf{e}_x) \hat{E})}_{\text{advection}} = 0, \quad (3)$$

where we have substituted for the GEOMETRIC prescription of  $\kappa_{\text{gm}}$  given by Eq. (1) into the eddy energy source term. The control variable for the present problem will be  $\lambda^{-1}(\phi, \theta)$ , and the state variable will be  $\hat{E}(\phi, \theta)$ . With a constraining model such as Eq. (3), we seek the optimal  $\lambda^{-1}(\phi, \theta)$  that minimizes the cost functional

$$J \equiv J_1 + J_2 = \frac{1}{A} \left\| \hat{E} - \hat{E}_{\text{data}} \right\|_{L^2}^2 + \epsilon \left\| \nabla_H \lambda^{-1} \right\|_{L^2}^2 \quad \left( \|f\|_{L^2}^2 = \int_A f^2 dA \right), \quad (4)$$

where  $A$  is the two-dimensional domain and  $dA$  is the area element. The optimization problem seeks for  $\hat{E}(\lambda^{-1})$  that is close to the diagnosed  $\hat{E}_{\text{data}}$  in the  $L^2$  norm (the spatial integral of the square of the mismatches), measured here by the cost functional  $J_1$ . Generally, optimization problems without a regularization term are ill-posed, leading to numerical non-convergence. For this work, we employ a Tikhonov-type regularization, introduced via a penalization term on the gradients of the control variable, given here by the cost functional  $J_2$ , with strength measure by some parameter  $\epsilon$ . Given that we are employing high resolution global circulation model data to infer for  $\lambda^{-1}(\phi, \theta)$  (which is a representation of the processes on a coarse resolution grid), the penalization term could be thought as our prior belief that our control variable should have broad spatial structures, or as a coarse-graining or averaging operation for the control variable  $\lambda^{-1}(\phi, \theta)$ . If  $\epsilon$  is too small, the optimization problem is trying to match per grid point, leading to extreme values in  $\lambda^{-1}(\phi, \theta)$  and sometimes numerical non-convergence.

Before we move on, we caveat that, by prescribing the dynamical variables, the constraining equation Eq. (3) is formally linear in the state variable  $\hat{E}$ . The resulting inference calculation then becomes relatively easy to implement and computationally inexpensive to perform, since this is essentially an optimization calculation subject to an elliptic partial differential equation under the present kinematic/diagnostic approximation. However, in a fully dynamical setting, the isopycnal slopes  $M^2/N^2$  for example would be regarded as an implicit function of  $\kappa_{\text{gm}}$ , which itself would be an explicit function of  $\hat{E}$  through the mesoscale eddy parameterization. The growth of  $\hat{E}$  will lead to an increase in  $\kappa_{\text{gm}}$ , which would lead to a flattening of the isopycnals, i.e. reductions in  $M^2$ , and the growth rate of the eddy energy would thus normally be self-limiting. Without dynamical feedbacks, the growth rate is expected to be over-estimated. Since we expect the dominant balance in the eddy energy equation Eq. (2)



to be between the source and dissipation term, for a fixed target  $\hat{E}_{\text{data}}$ , the present inference procedure is expected to return a  $\lambda^{-1}(\phi, \theta)$  with values that are too small (i.e., a dissipation time-scale that is too short). The results presented here should thus be viewed as a *lower bound* for  $\lambda^{-1}(\phi, \theta)$ . Some additional evidence in support of the proposed interpretation of the solutions as a lower bound is given in via prognostic calculations with full dynamical feedbacks in §4.

### 2.3 Forcing and target data diagnoses for inference calculation

For the proposed inference calculation, the forcing data we require are depth-integrated values of  $M^2$ ,  $N^2$ ,  $\tilde{\mathbf{u}}^z$ ,  $|c|$ , and the target  $\hat{E}_{\text{data}}$ . For this work, all the aforementioned variables were diagnosed from the nominally  $1/12^\circ$  horizontal resolution Nucleus for European Modelling of the Ocean (NEMO; Madec, 2008) ORCA0083-N01 hindcast outputs (see Data Availability section). Data used here were calculated from the five-day averaged outputs between and inclusive of the simulation years 2006 to 2010 (the last five years of the ORCA0083-N01 calculation), as depth-integrals on the native NEMO tri-polar grid (Madec & Imbard, 1996), and then time-averaged over the five year period.

The depth-integrated total eddy energy  $\hat{E}$  is computed as the sum of the depth-integrated eddy kinetic and potential energy. The depth-integrated (specific) eddy kinetic energy (with units of  $\text{m}^3 \text{s}^{-2}$ ) is defined in the usual fashion as

$$\text{EKE} = \frac{1}{2} \int_{-H}^0 (\overline{\mathbf{u} \cdot \mathbf{u}} - \bar{\mathbf{u}} \cdot \bar{\mathbf{u}}) dz, \quad (5)$$

where  $\overline{(\cdot)}$  is a time average. To obtain the analogous depth-integrated eddy potential energy, we take the five-day averaged temperature and salinity outputs, convert into neutral density  $\gamma^a$  co-ordinates via the McDougall and Jackett (2005) expression, re-bin the variables into an interval  $[\gamma_t^a = 1020 \text{ kg m}^{-3}, \gamma_b^a = 1029 \text{ kg m}^{-3}]$  (with smaller bin widths towards  $\gamma_b^a$ ), calculate the depth associated with the neutral density  $z(\gamma^a)$  every five days over the five year period, and compute

$$\text{EPE} = \frac{1}{2} \int_{\gamma_b^a}^{\gamma_t^a} g (\overline{z^2} - \bar{z}^2) d\gamma^a. \quad (6)$$

For the stratification parameters  $M^2/N$  and  $M^4/N^2$  as ratios, first we compute  $N^2$  and  $N$  as a three-dimensional field using the CDFTOOLS package from five-day averaged temperature and salinity data (using `cdfbn2`; see Data Availability section). A new program (`cdfsn2`) was created to mirror the NEMO computation of stratification gradient parameters, with code largely taken from the NEMO `ldfs1p` subroutine and dependencies. The new `cdfsn2` routine computes the isopycnal slopes  $M^2/N^2$  (`ws1p` in NEMO), appropriately modified by slope limiters, partial step corrections, and tapering as the lateral, mixed layer and surface boundaries are approached, and passed through a Shapiro filter in the horizontal. The intermediary  $N$  and  $N^2$  are then multiplied to the slope variables to obtain  $M^4/N^2$  and  $M^2/N$  as three-dimensional fields, which are then depth-integrated and time-averaged. The `cdfsn2` routine is able to reproduce the NEMO outputs directly up to very minor discrepancies (code tested on a simple re-entrant channel model and outputting the `ws1p` variable and its modifications directly).

The depth-averaged mean flow  $\tilde{\mathbf{u}}^z$  is computed in the usual way from the available data. The long Rossby phase speed  $|c|$  is computed as (e.g., Gill, 1982, Eq. 12.3.13)

$$|c| = \frac{c_1^2 \cos \theta}{2\Omega R_a \sin^2 \theta}, \quad c_1 = \frac{1}{\pi} \int_{-H}^0 |N| dz, \quad (7)$$

where  $\theta$  is the latitude,  $\Omega$  is the Earth’s angular frequency,  $R_a$  is the Earth’s radius, and  $c_1$  is an approximation of the first baroclinic phase speed (e.g. Nurser & Bacon, 2014). This phase speed is computed in this case from the time-averaged  $\int |N| dz$  field directly. One thing to note is that, because of the NEMO tri-polar grid, the  $(u, v)$  components of the velocity only correspond exactly to the zonal and meridional velocities when south of around  $20^\circ$  N (Madec & Imbard, 1996). While the anisotropy is relatively small, there are minor inconsistencies when interpolating data to and from the tri-polar grid. The effect of this error is not expected to be significant, since the advective contributions are expected to be rather minimal (and is supported by analyses presented in §3).

All the high resolution processed data on the tri-polar grid were additionally passed through a diffusion-based filter (Grooms et al., 2021) to smooth out variations smaller than twelve grid points, i.e. filtering to obtain the fields that are coherent over a nominally  $1^\circ$  horizontal resolution. This filtering step does not appear to be strictly necessary for the conclusions presented here, since the time-averaging operation already removes a substantial portion of the fluctuations below the  $1^\circ$  horizontal resolution for the variables of interest here (cf. Rai et al., 2021). Sample calculations without the filtering step led to no noticeable changes in the results presented.

## 2.4 Numerical implementation of inference problem

For the implementation of the inference calculation, we leverage the Firedrake software (Rathgeber et al., 2017), an automatic code generation framework with high level specification in Python that utilizes the finite element formalism (e.g., Durran, 2010, Ch.6). The procedure is that, given a finite element mesh, we specify the function space on which we seek our solution, taken to be continuous Galerkin with first-order Lagrange polynomials as the basis here. We then implement our constraining model in the weak form (e.g., Evans, 1998, Ch.1), which in this case involves multiply by a test function with sufficient differentiability such that integration by parts may be performed, and implement any natural or imposed boundaries on the problem accordingly. For a scalar test function  $\psi$ , the weak form  $\mathcal{F}(\hat{E}; \lambda) = 0$  associated with the constraining model Eq. (3) is given by

$$\mathcal{F}(\hat{E}; \lambda) \equiv \int_A \left[ \eta_E \nabla_H \hat{E} \cdot \nabla_H \psi + \left( \lambda \hat{E} - \alpha \frac{\int M^4/N^2 dz}{\int M^2/N dz} \hat{E} \right) \psi - \left( (\tilde{\mathbf{u}}^z - |c| \mathbf{e}_x) \hat{E} \cdot \nabla_H \psi \right) \right] dA = 0. \quad (8)$$

The boundary terms arising from integration by parts are identically zero from the boundary conditions for this problem, namely,  $\nabla_H \hat{E} \cdot \mathbf{n} = 0$  and no-normal flow conditions  $(\tilde{\mathbf{u}}^z - |c| \mathbf{e}_x) \cdot \mathbf{n} = 0$ , where  $\mathbf{n}$  is the vector perpendicular to the domain boundary  $\partial A$ . As opposed to the more conventional strong form formulation, where we seek a solution that satisfies Eq. (3) point-wise and the solution  $\hat{E}$  is required to be twice differentiable, the weak form formalism only requires a weak form solution  $\hat{E}$  to satisfy Eq. (8) in an integral sense, has weaker assumptions on differentiability, and the resulting problem is readily solved numerically within Firedrake.

Since Firedrake employs the finite element framework, we need a finite element mesh. For this work a choice was made to solve the problem on a two-dimensional spherical mesh embedded into the standard three-dimensional Euclidean space  $\mathbb{R}^3$ , where the relevant periodicities and land boundaries are built into the mesh itself (as opposed to constructing a longitude-latitude grid with North Pole folding, which leads to a point singularity). An unstructured mesh with triangular elements with characteristic length-scale 100 km was created using the `Qmesh` package (Avdis et al., 2018), with the land shape generated from the NEMO ORCA1 configuration (a global ocean configuration with a nominal horizontal resolution of  $1^\circ$ ). To move the diagnosed



data from the tri-polar NEMO grid onto the mesh, a simple change of co-ordinates from  $(\phi, \theta)$  to  $(x, y, z)$  and linear interpolation (through the Python `scipy` package) was performed, with extrapolations where necessary (e.g. near the geographical locations associated with the edges of the tri-polar grid). Note that while interpolating scalars is straight-forward, interpolating vectors require preserving both the direction and magnitude, which can be achieved via a multiplication by a rotation matrix.

Once we have data on the mesh, and upon specification of the parameters, we can proceed to build the constraint model, couple the model to an optimizer in Firedrake, and solve the resulting optimization problem. For numerical stability reasons, in order to obtain physical solutions, we modify Eq. (8) by adding a term  $\hat{E}_0$  that maintains a minimum energy value, and replacing  $\hat{E}$  by  $\hat{E}_{\text{data}}$  in the source term so that the source term becomes a diagnostic variable, i.e. we solve

$$\begin{aligned} \mathcal{F}(\hat{E}; \lambda) \equiv & \int_A \left[ \eta_E \nabla_H \hat{E} \cdot \nabla_H \psi + \left( \lambda(\hat{E} - \hat{E}_0) - \alpha \frac{\int M^4/N^2 dz}{\int M^2/N dz} \hat{E}_{\text{data}} \right) \psi \right. \\ & \left. - \left( (\tilde{\mathbf{u}}^z - |c| \mathbf{e}_x) \cdot \hat{E} \cdot \nabla_H \psi \right) \right] dA. \end{aligned} \quad (9)$$

For the first modification, adding a  $\hat{E}_0 > 0$  term is necessary for the numerical solver to converge to a non-zero solution in the absence of the second modification, otherwise its role is to ensure the solution  $\hat{E}$  has a minimum background value, consistent with how GEOMETRIC is currently implemented into NEMO (Mak et al., 2022). The second modification is perhaps a more severe one, and arises most likely because we are forcing the present inference problem with prescribed data and removing dynamical feedbacks by construction. With full dynamical coupling, the stratification responds to changing  $\hat{E}$  via the GEOMETRIC parameterization, and is a self-limiting process that arrests the growth of  $\hat{E}$ . In the present setup, this is not possible since the dynamical variables are prescribed, and the form of the growth term implies exponential growth of  $\hat{E}$  during the iterations (through time-stepping or an iterative solver). Any imbalance in the initialization of the data will be amplified exponentially during the iterations. The imbalance will generically occur in the present set up, since the data diagnosed from ORCA0083-N01 will certainly not be in exact steady state, and we do not have the perfectly matched  $\lambda^{-1}(\phi, \theta)$  and  $\hat{E}$  at the initialization stage, since that necessarily implies we have the solution before even solving the problem. Solving Eq. (8) as is leads to significant over/undershoots, with very large positive and negative values in  $\hat{E}$ ; during the development of the present work, a channel model simulation could be integrated to equilibrium, and the described problem was lessened though not completely circumvented. Replacing  $\hat{E}$  by  $\hat{E}_{\text{data}}$  in Eq. (9) acts as a numerical stabilizer that limits the amount of growth possible. The consequences of the approximation and how to alleviate it will be discussed in §5.

To solve the optimization problem where we minimize the cost functional Eq. (4) subject to the model given by Eq. (9), we employ the `tlm_adjoint` library (Maddison et al., 2019) with the Firedrake wrapper, which allows us to build the constrained optimization problem in Firedrake. The optimization problem is solved using a L-BFGS (Limited memory Broyden–Fletcher–Goldfarb–Shanno) algorithm, which is a quasi-Newton method that looks for descents through an estimate of the inverse Hessian matrix (e.g., Byrd et al., 1995). As demonstration, the actual production code used for implementing the elliptic solve for Eq. (9), forming the cost functional Eq. (4) and wrapping to the optimizer is given in Fig. 1. Aside from the fact this code is incredibly short and required minimal time to write, the optimization and inference calculations become flexible since any changes in the problem statement are automatically propagated to the optimizer routines via automatic code generation capabilities. For example, if we want to modify the cost functional (e.g. changing the measure of the mismatch, changing the existing Tikhonov-type regularization, adding extra penalization terms), then we simply modify the relevant lines defining  $J$ . If we want to modify

```

def forward(lam):
    Edz = Function(P, name = "Edz")
    F = ( + Constant(alp) * Etot_zint * N_over_M2 * M4_over_N2 * test * dx # source
          - lam * ( Edz - Constant(E0) ) * test * dx # dissipation
          - Constant(nu) * dot( grad(Edz), grad(test) ) * dx # diffusion
          + dot(Edz * u_zavg, grad(test)) * dx # advection
        )

    solve(F == 0, Edz, solver_parameters = sp) # magic inherited from Patrick F.
    J = Functional(name="J") # cost functional: mismatch + regularisation
    J1 = (1.0 / domain_area) * inner(Edz - Etot_zint, Edz - Etot_zint) * dx
    J2 = Constant(eps) * inner(grad(lam), grad(lam)) * dx
    J.assign(J1 + J2)
    return Edz, J

lam = Function(P, name = "lam"); lam.assign(Constant(lam_s)) # initial guess
start_manager(); _, J = forward(lam); stop_manager() # start tape
def forward_J(lam): # define function to optimise: J = forward(lam)
    return forward(lam)[1]
lam_opt, result = minimize_scipy(forward_J, lam,
                                method="L-BFGS-B",
                                options={"disp": True, "maxiter": 100})

```

**Figure 1.** Firedrake driver code for solving the optimization problem that minimizes the cost functional Eq. (4) subject to Eq. (9). The code defines the weak form, solves it with some specified solver parameters, and defines the cost functional. The `tlm_adjoint` equation manager is then called, and passes the defined cost functional  $J = \mathcal{F}(\lambda^{-1})$  to the optimization algorithm.

the constraining model (e.g. remove advection, employ quadratic dissipation, spatially varying  $\alpha$ , increasing the number of control variables, use another choice of eddy energy equation), we re-define the weak form  $F$  and/or the control variables accordingly, as long as if we have relevant diagnostic inputs to force the resulting equations.

As a final note, while the inference calculation is carried out on the spherical mesh, it is desirable to transform data onto a regular longitude-latitude grid for further analyses, and necessary to put data on NEMO ORCA1 tri-polar grid to test out consequences of employing the inferred  $\lambda^{-1}(\phi, \theta)$  in prognostic calculations. A technical complication arises here that the spherical mesh is an immersed manifold (a sub-manifold of the 2-sphere  $S^2$  embedded in  $\mathbb{R}^3$ ), which has zero measure in the embedding space ( $S^2$  has no ‘volume’). The standard procedure of probing the function values on the immersed manifold will fail as it is mathematically ill-defined: the probability of a given co-ordinate point being on the manifold is related to the measure, and an arbitrary co-ordinate point we wish to query the function value at will almost surely not be on the zero-measure manifold. One way round this technical issue is to probe the finite element output using the `vtk` package directly, locating the cell closest to the co-ordinate of the point being queried, project that point onto the cell, which is now regarded as a sub-manifold of  $\mathbb{R}^2$  (the measure of interest is now ‘area’), and the function can then be queried accordingly. For the analyses presented in §3, all relevant mesh data was interpolated onto a regular latitude-longitude grid with  $1/4^\circ$  spacing for ease of visualization. For the prognostic calculations in §4, the inferred  $\lambda^{-1}(\phi, \theta)$  was interpolated directly from the spherical mesh onto the NEMO ORCA1 tri-polar grid.

**Table 1.** Parameter values employed in the inference problem. The boldfaced values denote the control calculation.

Parameter	Values	Units
$\alpha$	0.04	—
$\eta E$	500	$\text{m}^2 \text{s}^{-1}$
$\hat{E}_0$	4.0	$\text{m}^3 \text{s}^{-2}$
$\lambda_0^{-1}$	365	days
$\epsilon$	$a \times 10^b$	$\text{m}^8 \text{s}^{-2}$
	$a \in \{1, \mathbf{5}\}, b \in \{13, 14, \mathbf{15}, 16\}$	

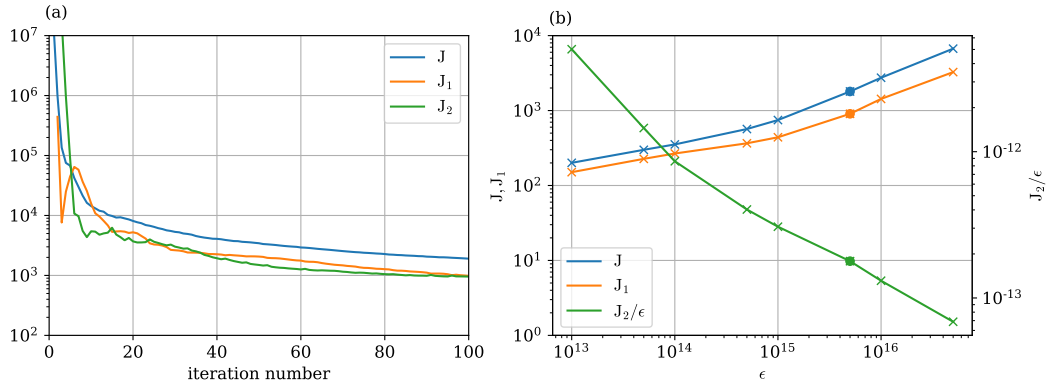


**Figure 2.** Behavior of the cost functional Eq. (4) as a function of (a) iterations for the  $\epsilon = 5 \times 10^{15}$  calculation, and (b) as a function of  $\epsilon$ . The markers denote the parameters with calculations, and the solid circle marker denotes the control calculation.

### 3 Analysis of inferred dissipation time-scale $\lambda^{-1}(\phi, \theta)$

Inference calculations for  $\lambda^{-1}(\phi, \theta)$  with the cost functional Eq. (4) subject the constraint Eq. (9) were performed using the parameters in Table 1, with values chosen partly to coincide with those used in the prognostic calculations documented in Mak et al. (2022). All optimization calculations were initialized with a spatially uniform initial condition of  $\lambda_0^{-1} = 365$  days and  $\hat{E} = 0$ . Of principal interest here is the control calculation utilizing  $\epsilon = 5 \times 10^{15}$ .

For the optimization calculations, the default convergence criterion based on projected gradients or the differences in function values were not triggered, though it is clear that the values of the cost functional are converging to some asymptotic value (albeit rather slowly); see for example Fig. 2a for the control calculation as a function of the iteration number. For consistency reasons, all results relating to the optimization calculation reported in this work were taken to be the solution at the 100<sup>th</sup> iteration. The corresponding run time for each calculation was around three minutes on a laptop (the one utilized for this work has Intel i7 CPUs and a RAM capacity of 8 GB). Fig. 2b shows the dependence of the cost functional  $J$  and its components on the value of  $\epsilon$ . As expected, with increasing  $\epsilon$ , gradients in the optimized solution, proportional to the numerical value of  $J_2$ , are penalized, at the expense of having larger mismatches between the target  $\hat{E}_{\text{data}}$  and the state variable  $\hat{E}(\lambda^{-1})$ , encoded by  $J_1$ .

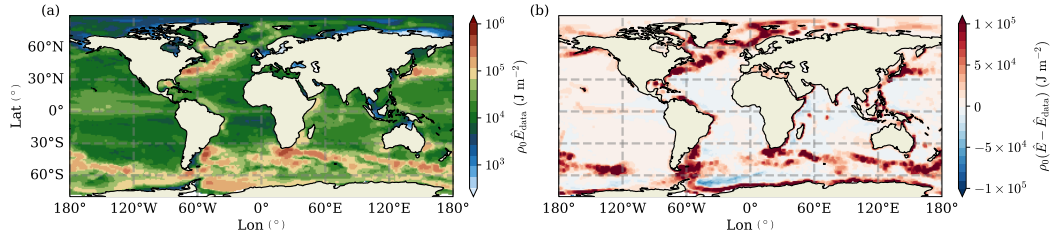


**Figure 3.** (a) The diagnosed depth-integrated eddy energy target  $\rho_0 \hat{E}_{\text{data}}$  and (b) the signed mismatch  $\rho_0(\hat{E} - \hat{E}_{\text{data}})$  associated with  $\lambda^{-1}(\phi, \theta)$  with  $\epsilon = 5 \times 10^{15}$ . Here we take  $\rho_0 = 1026 \text{ kg m}^{-3}$ , and the variables are in units of  $\text{J m}^{-2}$ .

Fig. 3 shows the target  $\hat{E}_{\text{data}}$  and the signed mismatch  $\hat{E} - \hat{E}_{\text{data}}$  of the control calculation as a function of longitude and latitude. The target  $\hat{E}_{\text{data}}$  is that diagnosed from the eddy resolving calculation ORCA0083-N01 (cf. Fig. 5a of Mak et al., 2022), showing a large eddy energy signature in the Southern Ocean and Western Boundary Currents, and lower eddy activity in the Arctic and the ocean basins. From the signed mismatch, the eddy energy signature associated with the inferred solution is generally larger than the target. If  $\epsilon$  is decreased in magnitude, the local signed mismatches shown in Fig. 3b decreases in magnitude, with negligible changes in the position; however, that results in larger gradients and more extreme values in  $\lambda^{-1}(\phi, \theta)$ , with the local signed mismatches still largely skewed towards positive values. Recalling from §2, the stratification is prescribed in this work, thus forbidding dynamical adjustments, and the positive skew observed here indicates that the now prescribed eddy energy growth rate is still too large, requiring the  $\lambda^{-1}(\phi, \theta)$  to take smaller values to increase the dissipation to balance the growth rate. As argued in §2, in a dynamically constrained inference, the eddy energy growth rate will be arrested by the dynamical slumping of isopycnals, so that the resulting values of  $\lambda^{-1}(\phi, \theta)$  would not be as small, and reinforces the interpretation that our inferred solution should be seen as a lower bound.

The eddy energy dissipation time-scale  $\lambda^{-1}(\phi, \theta)$  for the control calculation is shown in Fig. 4. With regards to spatial distribution, the values are small (i.e. short dissipation time-scale) within the Southern Ocean (particularly in the Atlantic and Indian sectors), around the Western Boundary Currents, and on the western ocean-land boundaries. On the other hand, the values are large (i.e. long dissipation time-scale) generally in the equatorial regions, but more wide spread in the Eastern Pacific. The geographical locations of short eddy energy dissipation time-scale are perhaps not surprising, given that these are regions with strong flows and vigorous baroclinic eddy activity (cf. Fig. 3a in the depth-integrated total eddy energy signature). The Southern Ocean and the Western Boundary Currents are strongly turbulent regions, with significant mean flows in the presence of rough bathymetry, leading to large eddy energy dissipation via the multitude of dynamical processes given in §1. The western boundary intensification of eddy energy dissipation is consistent with the findings of Zhai et al. (2010), resulting from eddy energy convergence at the western boundaries via propagation of eddies at the long Rossby wave phase speed (Chelton et al., 2011; Klocker & Marshall, 2014), with energy being transferred out of the geostrophic scales by processes such as loss of balance and non-propagating form drag (Z. Yang et al., 2021). The long dissipation time-scales observed in the tropical regions and in the Eastern Pacific is also consistent with expectations, as these are regions where baroclinic instability is not expected to be particularly prevalent.

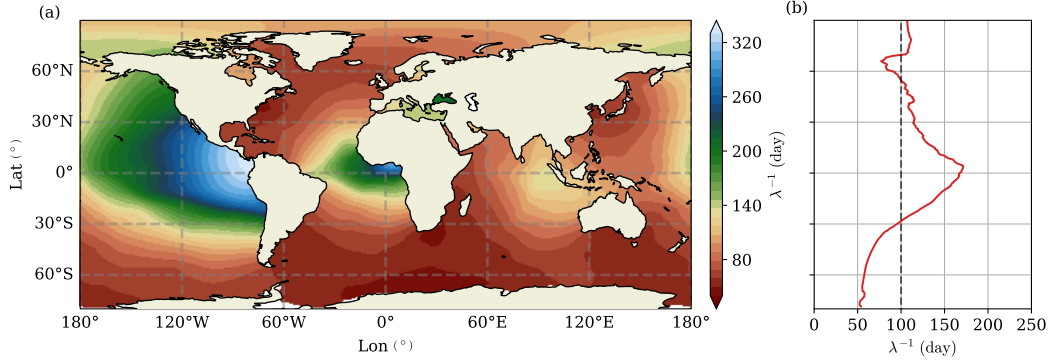


**Figure 4.** Optimized  $\lambda^{-1}(\phi, \theta)$  for the  $\epsilon = 5 \times 10^{15}$  calculation. (a)  $\lambda^{-1}(\phi, \theta)$  in units of days. (b) the zonal average of  $\lambda^{-1}(\phi, \theta)$ , with the constant value of  $\lambda^{-1} = 100$  days as used in the prognostic calculations of Mak et al. (2022) is marked as the dashed gray line.

Fig. 5a–d shows the representative features in the inferred  $\lambda^{-1}(\phi, \theta)$  for varying  $\epsilon$ . While calculations at different values of  $\epsilon$  possess qualitatively similar spatial distributions, for lower values of  $\epsilon$ , the solution is allowed to take more extreme values and the resulting values of  $\lambda^{-1}(\phi, \theta)$  is generally smaller, while the converse is true. Fig. 5e, f shows the result of a calculation where we take  $\epsilon = 5 \times 10^{15}$  but exclude the advective contribution in the inference calculation (by commenting out the last line defining  $\mathbf{F}$  in Fig. 1 when performing the optimization calculation). The resulting spatial and zonal distribution is largely similar to the solutions with advection, but with reduced western intensification, particularly in the Western Pacific, Indian subtropics and Eastern Australia, attributed to lack of eddy energy advection westward at the long Rossby phase speed. The inclusion of advection leads to local differences in the distribution of the eddy energy and thus  $\lambda^{-1}(\phi, \theta)$ , but with only minor difference to the overall magnitudes in its zonal average.

The parameters chosen for the calculations given in Table 1 were motivated by the choices made in prognostic calculations of (Mak et al., 2022) with NEMO ORCA1 employing GEOMETRIC, though we are free to explore the parameter space for the inference calculation. It is found that if we increase the horizontal eddy energy diffusion coefficient  $\eta_E$  for fixed  $\epsilon$ , the model given by Eq. (9) outputs a  $\hat{E}$  that is weaker and more diffused, and the optimizer returns a  $\lambda^{-1}(\phi, \theta)$  with similar spatial distributions but marginally larger values. Increasing  $\hat{E}_0$  by no more than an order of magnitude for fixed  $\epsilon$  leads to very mild effects in the basin regions where  $\hat{E}$  is small. Increasing  $\alpha$  for fixed  $\epsilon$  leads to globally smaller values of  $\lambda^{-1}(\phi, \theta)$ , since  $\alpha$  affects the growth term in Eq. (9), and thus calls for larger eddy energy dissipation to maintain balance. Beyond the eddy energy equation parameters, if  $\epsilon \lesssim 10^{13}$ , the optimization calculation starts to have large variations in  $\lambda^{-1}(\phi, \theta)$  and can return negative values of  $\hat{E}$ ; such results were deemed unphysical and have been omitted from this work. While we employ a finite element mesh with a horizontal characteristic length scale of 100 km, changing the mesh resolution itself has very little influence on the solutions as long as  $\epsilon$  is larger than about  $10^{14}$ , but with a significant increase in computation cost mostly from memory requirements (through the elliptic solve rather than the L-BFGS-B algorithm). The reason for the relative invariance of the solution to the finite element mesh resolution is from the fact that the current inference problem is diagnostic in nature, and it is the resolution of the model generating the forcing data for the inverse calculation that has the most effect.

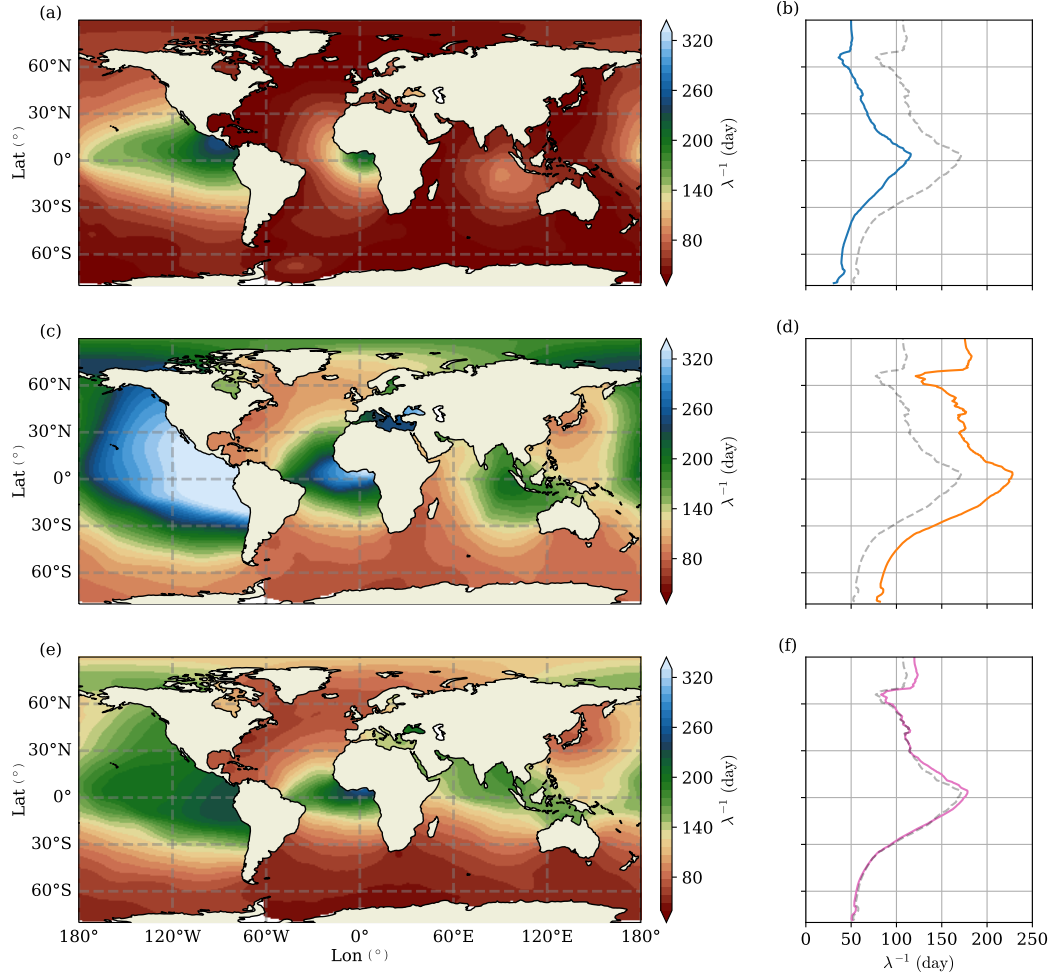


**Figure 5.** (a, c, e) Inferred  $\lambda^{-1}(\phi, \theta)$  (with red denoting larger eddy energy dissipation) and (b, d, f) its zonal average, where the dashed gray line denotes the control calculation  $\epsilon = 5 \times 10^{15}$ . (a, b)  $\epsilon = 1 \times 10^{14}$ ; (c, d)  $\epsilon = 5 \times 10^{16}$ ; (e, f)  $\epsilon = 5 \times 10^{15}$  but with no advection contributions.



## 4 Prognostic model calculations

The presence of feedback loops means there is no guarantee that a diagnostic result such as the one here will lead to improvements in a prognostic calculation. The inferred  $\lambda^{-1}(\phi, \theta)$  is thus utilized as a prescribed input is utilized in an ocean global circulation model in prognostic mode, to assess the consequences on the model output and behavior compared with the case where a prescribed spatially constant  $\lambda^{-1}$  field is used (cf. Mak et al., 2022). The principal hypothesis is that the use of  $\lambda^{-1}(\phi, \theta)$  will improve on the resulting parameterized total eddy energy signature. A secondary aim is a demonstration that the inferred  $\lambda^{-1}(\phi, \theta)$  is a physically plausible lower bound for the mesoscale eddy energy dissipation time-scale.

The model and set up we employ is exactly the same as one in Mak et al. (2022). An ocean only global configuration model employing NEMO (Madec, 2008, v3.7dev r8666) using a tri-polar grid ORCA1 grid (Madec & Imbard, 1996) with nominally  $1^\circ$  horizontal resolution (ORCA1) with the LIM3 ice model (Rousset et al., 2015) is utilized. With 46 uneven vertical levels, placing more resolution near the ocean surface, the model employs the TEOS-10 equation of state (Roquet et al., 2015). Forcing by the atmosphere is modeled by the NCAR bulk formulae with normal year forcing (Large & Yeager, 2009). Sea surface salinity but not temperature restoration is included to reduce model drift. The GEOMETRIC implementation in NEMO for this model is described in Mak et al. (2022), and is essentially given by Eq. (2) here, with the addition of the  $E_0$  term (cf. Eq. 9). The parameters chosen for the prognostic calculations are exactly those given in Table 1. The model is spun up from WOA13 climatology (Locarnini et al., 2013; Zweng et al., 2013) for 300 years. Prognostic calculations with  $\lambda^{-1}(\phi, \theta)$  for  $\epsilon = 5 \times 10^{15}$  and  $\epsilon = 5 \times 10^{16}$  (cf. Fig. 4 and 5b) are reported here; the calculation with  $\lambda^{-1}(\phi, \theta)$  for  $\epsilon = 1 \times 10^{14}$  (cf. Fig. 5a) was found to be numerically unstable in the parameterized eddy energy equation and has been omitted.

Denoting  $\langle \cdot \rangle$  to be the domain-integrated quantity, we first show in Fig. 6 the time-series of the calculation utilizing  $\lambda^{-1}(\phi, \theta)$  with  $\epsilon = 5 \times 10^{15}$  for the diagnosed domain-integrated eddy energy  $\langle \rho E \rangle$ , the total and thermal wind component of the Antarctic Circumpolar Current transport  $T_{\text{ACC}}$  (where the total is the transport over the whole depth of the Drake passage, and the thermal wind component is calculated as the residual of the total and the analogous depth-integrated bottom flow), and the total ocean heat content  $\langle \rho c_p \Theta \rangle$ , where  $\rho$  is the locally referenced density,  $c_p$  is the heat capacity, and  $\Theta$  is the conservative temperature. The main purpose here is to demonstrate the multiple adjustment time-scales inherent in the different diagnosed quantities. The parameterized eddy energy as represented through GEOMETRIC here adjusts on a fast time-scale (of around 5 to 10 years), while the  $T_{\text{ACC}}$  might be argued to have reached a quasi-equilibrium over centennial time-scales but, like the ocean heat content, there is a much longer adjustment on millennium time-scales associated with the deep/abyssal stratification (e.g. Mak et al., 2022).

With these observations in mind, for simplicity and computation resource reasons, we will make a direct comparison of the present calculations employing  $\lambda^{-1}(\phi, \theta)$  where diagnostics were averaged over the model years 290 to 300, with the previously reported results of Mak et al. (2022) employing a spatially constant  $\lambda^{-1} = 100$  days that already exists, but where the data was diagnosed from averages over the model years 3000 to 3100. For comparing the eddy energy signature this should not be an issue, given both calculations have a parameterized (domain-integrated and spatially varying) eddy energy signature that will have equilibrated. For comparing circulation metrics such as  $T_{\text{ACC}}$  and the Atlantic Meridional Overturning Circulation  $T_{\text{AMOC}}$ , the diagnosed values can be compared as long as we bear in mind that there will likely be 10 to 20% upward drift of  $T_{\text{ACC}}$  and  $T_{\text{AMOC}}$  in the present results until equilibra-

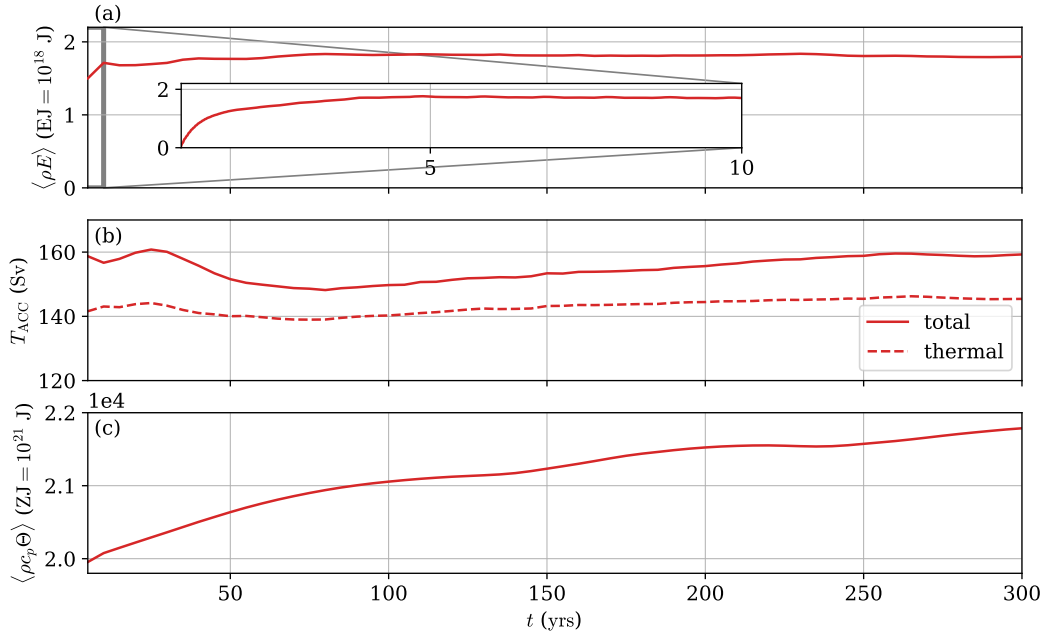


**Figure 6.** Time-series of the prognostic calculation employing the inferred  $\lambda^{-1}(\phi, \theta)$  with  $\epsilon = 5 \times 10^{15}$ . (a) Domain integrated eddy energy  $\langle \rho E \rangle$  from GEOMETRIC (in units of  $EJ = 10^{18}$  J, with  $\rho_0 = 1026 \text{ kg m}^{-3}$ ), with inset showing the same quantity at higher temporal resolution over the first 10 years. (b) Antarctic Circumpolar Current transport  $T_{ACC}$  with total and thermal wind component (in units of Sverdrups), where thermal wind component defined as the residual of the total minus the depth-integrated bottom flow transport. (c) Domain-integrated ocean heat content  $\langle \rho c_p \Theta \rangle$ , where  $\rho$  is the locally referenced density,  $c_p$  is the heat capacity, and  $\Theta$  is the conservative temperature.

**Table 2.** Computed diagnostics of the calculations employing spatially constant  $\lambda^{-1}$  (100 days, data from Mak et al., 2022) and calculations employing the inferred  $\lambda^{-1}(\phi, \theta)$  for  $\epsilon = 5 \times 10^{15}$  and  $5 \times 10^{16}$  (the prognostic calculation for  $\epsilon = 1 \times 10^{14}$  was numerically unstable and omitted). Diagnostics are:  $J_3$ , the area averaged mismatch of the depth-integrated eddy energy as compared to the analogous ORCA0083-N01 reference calculation;  $\langle \rho E \rangle$ , the domain-integrated eddy energy from the prognostic calculations;  $T_{\text{ACC}}$ , the Antarctic Circumpolar Current transport (total and thermal wind component), diagnosed as the transport over the model Drake passage;  $T_{\text{AMOC}}$  diagnosed as the northward transport over the top 1000 m at  $26^\circ$  N at the Western side of the Atlantic. For reference, ORCA0083-N01 has  $\langle \rho E_{\text{data}} \rangle = 9.52$  EJ.

	$J_3$ ( $\text{m}^3 \text{s}^{-2}$ )	$\langle \rho E \rangle$ (EJ = $10^{18}$ J)	$T_{\text{ACC}}$ (Sv)	$T_{\text{AMOC}}$ (Sv)
$\lambda^{-1} = 100$ days (Mak et al., 2022)	1922.22	3.33	138.10 (total) 121.23 (thermal)	10.38
$\lambda^{-1}(\theta, \phi)$ ( $\epsilon = 5 \times 10^{15}$ )	1560.89	1.80	159.17 (total) 145.41 (thermal)	11.13
$\lambda^{-1}(\theta, \phi)$ ( $\epsilon = 5 \times 10^{16}$ )	1954.70	2.98	143.27 (total) 99.29 (thermal)	9.05

tion occurs over the 500 to 1000 year time-scale. We refrain from comparing the ocean heat content.

To quantify whether our choice of  $\lambda^{-1}(\phi, \theta)$  is able to improve the eddy energy signature, we take  $\hat{E}_{\text{data}}$  as diagnosed from ORCA0083-N01 (interpolated onto the ORCA1 grid) as the reference, and compute the area-averaged  $L^2$  mismatch of the corresponding  $\hat{E}_{\text{ORCA1}}$  from the prognostic calculations, given by

$$J_3 = \frac{1}{A} \|\hat{E}_{\text{data}} - \hat{E}_{\text{ORCA1}}\|_{L^2}^2 = \frac{1}{A} \int_A \left( \hat{E}_{\text{data}} - \hat{E}_{\text{ORCA1}} \right)^2 dA. \quad (10)$$

We additionally compute the domain-integrated total eddy energy value  $\langle \rho E \rangle$ , the total and thermal wind component of  $T_{\text{ACC}}$ , and the Atlantic Meridional Overturning Circulation  $T_{\text{AMOC}}$  (diagnosed as the northward transport over the top 1000 m at  $26^\circ$  N at the Western side of the Atlantic). The computed diagnostics are given in Table 2.

From the computed values of  $J_3$ , it may be seen that the calculation using  $\lambda^{-1}(\phi, \theta)$  with  $\epsilon = 5 \times 10^{15}$  has a lower  $L^2$  mismatch compared to the calculation with  $\epsilon = 5 \times 10^{16}$  and the one with spatially constant  $\lambda^{-1}$ , although arguably the improvements are somewhat modest. Fig. 7 shows the spatial distribution of the signed mismatch, and the lower values of  $J_3$  from the prognostic calculations using  $\lambda^{-1}(\phi, \theta)$  with  $\epsilon = 5 \times 10^{15}$  compared to the calculation with  $\lambda_0^{-1} = 100$  days results primarily come from improvements within the Southern Ocean, where the prognostic calculations using  $\lambda^{-1}(\phi, \theta)$  has reduced coverage of positive biases in the depth-integrated eddy energy. The reduction in the average values of the eddy energy  $\langle \rho E \rangle$  can also be seen to be arising from the reduced values of the eddy energy in the Southern Ocean.

The negative biases however are generally large, as can be seen in Fig. 7. Additionally, note that the domain-integrated eddy energy value of the reference ORCA0083-N01 calculation is  $\langle \rho E_{\text{data}} \rangle = 9.52$  EJ, and the corresponding values from the prognostic calculations given in Table 2 are a few factors lower. While the Southern Ocean biases have been reduced somewhat, over the rest of the globe the negative bias is

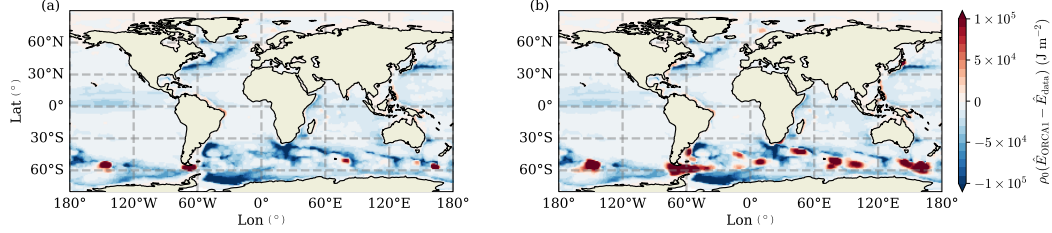


**Figure 7.** Spatial distribution of the signed mismatch  $\rho_0(\hat{E}_{\text{ORCA1}} - \hat{E}_{\text{data}})$ , where  $\rho_0 = 1026 \text{ kg m}^{-3}$ , so data is now in units of  $\text{J m}^{-2}$ . Both simulations employ the standard normal year forcing with no amplified wind, with (a) utilizing  $\lambda^{-1}(\phi, \theta)$  with  $\epsilon = 5 \times 10^{15}$  (cf. Fig. 4), and (b)  $\lambda_0^{-1} = 100$  days everywhere.

prevalent, which is somewhat consistent with an eddy energy dissipation time-scale that is too short.

Beyond the response in the eddy energy signature, the calculations with  $\lambda^{-1}(\phi, \theta)$  also results in a plausible  $T_{\text{ACC}}$  as well as  $T_{\text{AMOC}}$ , although the latter is a little on the low side; see for example Table 2 in Farneti et al. (2015) and Fig. 1 of Danabasoglu et al. (2014) for a summary of model and observational estimates for  $T_{\text{ACC}}$  and  $T_{\text{AMOC}}$  respectively. It should be noted that the calculation using  $\lambda^{-1}(\phi, \theta)$  with  $\epsilon = 5 \times 10^{15}$  has the highest  $T_{\text{ACC}}$  (both total and thermal wind component) and  $T_{\text{AMOC}}$ . This is consistent with expectations, since the associated dissipation time-scale in the Southern Ocean is the shortest, leading to reduced flattening of isopycnals by mesoscale eddies, steeper stratification in the Southern Ocean (D. P. Marshall et al., 2017; Mak et al., 2018), and in turn a deepening of the global pycnocline and increased  $T_{\text{AMOC}}$  via isopycnal connectivity (D. P. Marshall & Johnson, 2017), something that has been demonstrated in numerical models (Mak et al., 2018, 2022). The results here also provide some additional evidence for the interpretation that the  $\lambda^{-1}(\phi, \theta)$  given here should be viewed as a lower bound, since  $T_{\text{ACC}}$  is already on the rather high side.

It may be of interest to consider the statistical distribution in addition to the spatial distribution of the eddy energy dissipation. We note that the work of Pearson and Fox-Kemper (2018) reports that the dissipation of eddy kinetic energy in a high resolution global ocean model follows a log-normal distribution on horizontal slices, with slightly varying statistics in depth, and makes the point that mesoscale parameterizations should be such that the energy flux statistics are consistent with the reported diagnostics. We show in Fig. 8 the probability distribution function (PDF) of the depth-averaged eddy energy dissipation as parameterized, given by

$$\tilde{\Lambda}^z = \frac{1}{H} \left( \lambda \int_0^H (E - E_0) dz \right), \quad (11)$$

which has units of  $\text{m}^2 \text{ s}^{-3}$  like the turbulent energy flux in Pearson and Fox-Kemper (2018), for the prognostic calculation using  $\lambda^{-1}(\theta, \phi)$  with  $\epsilon = 5 \times 10^{15}$  as well as for the case with uniform  $\lambda^{-1} = 100$  days.

A direct comparison of the results here with the work of Pearson and Fox-Kemper (2018) is slightly problematic in the sense that the quantities to be compared are different (depth-integrated dissipation of eddy kinetic and potential energy here as compared to horizontal slices of eddy kinetic energy dissipation), but nevertheless the values of the energy dissipation obtained here are not unreasonable compared to Fig. 1 of Pearson and Fox-Kemper (2018), although our dissipation is on the larger side. While there are hints of log-Gaussianity in our PDFs, there is also notable

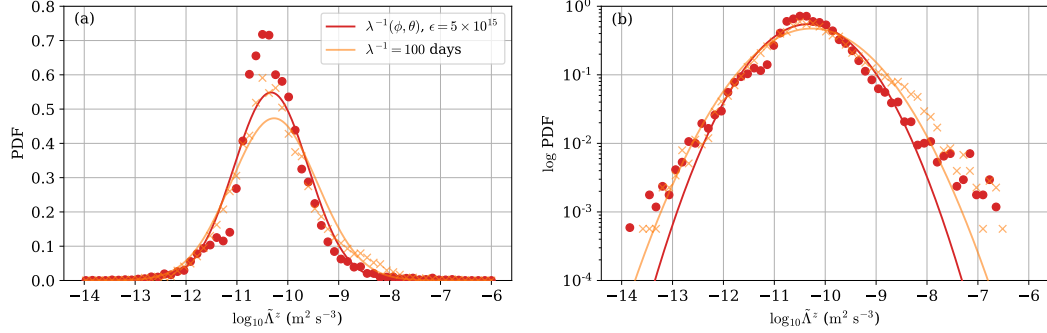


**Figure 8.** The PDF of the depth-averaged total eddy energy dissipation from the calculation utilizing  $\lambda^{-1}(\phi, \theta)$  with  $\epsilon = 5 \times 10^{15}$  (red) and  $\lambda_0^{-1} = 100$  days everywhere (orange), for diagnosed data (markers) and the best-fit Gaussian PDF (lines). The PDF shows one particular snapshot from five day averaged data within the averaging period of the respective prognostic calculation, but is representative of other sampled time snapshots as well as similar to the analogous PDF from time-mean data. (a) The PDF of the  $\log_{10} \tilde{\Lambda}^z$  given in Eq. (11). (b) Same as (a) but on a base 10 logarithmic scale.

skewness to the larger values, as well as kurtosis in the data reflected by the heavy tails, as can be seen in Fig. 8b with the distribution of data points relative to the best fit log-Gaussian PDF. The use of  $\lambda^{-1}(\phi, \theta)$  with  $\epsilon = 5 \times 10^{15}$  additionally leads to a reduction in the variance and larger dissipation values compared to the case with spatially uniform  $\lambda^{-1}$ , as seen by the relatively more narrow best-fit PDF, and a noticeable dip in the values of the data points at the higher end of the distribution. The observed relative differences may be attributed to a significant decrease in the positive biases of eddy energy signatures in the Southern Ocean where dissipation is strong. Our interpretation that  $\lambda^{-1}(\phi, \theta)$  is expected to be a lower bound in the time-scale is somewhat consistent with the observation that our dissipation rate is possibly on the larger side compared to the values reported in Pearson and Fox-Kemper (2018).

## 5 Conclusions and outlooks

In this work we provide a leading order constraint for the spatial distribution of eddy energy flux out of the geostrophic mesoscales, interpreted here as a geostrophic mesoscale eddy energy dissipation time-scale  $\lambda^{-1}(\phi, \theta)$ . The problem is viewed as one of parameter inference for  $\lambda^{-1}(\phi, \theta)$ , here inferred from high resolution numerical model data and constrained by a parameterized eddy energy equation, as a precursor for the more complete dynamically constrained inference problem utilizing ocean observational data, to be discussed below. A simple and computationally inexpensive optimization problem was performed, seeking an optimal  $\lambda^{-1}(\phi, \theta)$  that minimizes the mismatch between the depth-integrated total eddy energy from the parameterized eddy energy equation  $\tilde{E}(\lambda^{-1})$  and the depth-integrated total eddy energy diagnosed from a high resolution numerical model  $\tilde{E}_{\text{data}}$ . The present implementation utilizes the Firedrake software, leveraging the inbuilt solvers as well as the automatic code generation capabilities to solve and explore the associated optimization problem and its sensitivities to parameter choices. The inferred  $\lambda^{-1}(\phi, \theta)$  has the smallest values within the Southern Ocean, Western Boundary Currents, and is western boundary intensified, regions where baroclinic turbulence is particularly dominant, and coinciding with where we expect the greatest energy flux out of the geostrophic mesoscales from dynamical considerations (e.g. Zhai et al., 2010; Nikurashin & Ferrari, 2011; Melet

et al., 2015; Rocha et al., 2018; Rai et al., 2021). We caveat that while the inferred spatial distribution of  $\lambda^{-1}(\phi, \theta)$  may be consistent with expectations, the resulting magnitudes should be viewed as a physically plausible lower bound.

Prognostic calculations utilizing the inferred  $\lambda^{-1}(\phi, \theta)$  in the coarse resolution global configuration ocean model NEMO ORCA1 were performed. The coarse resolution calculations result in an improved mismatch in the parameterized depth-integrated eddy energy signature in the globally integrated  $L^2$  sense compared to a previous work that employs a spatially constant  $\lambda^{-1} = 100$  days also in NEMO ORCA1 (Mak et al., 2022), where the reference eddy energy signature is diagnosed from the high resolution calculation NEMO ORCA0083-N01. The use of  $\lambda^{-1}(\phi, \theta)$  reduces positive biases in total eddy energy signature in the Southern Ocean, though negative biases remain prevalent throughout the globe, and the coarse resolution calculation possesses an average eddy energy value that is too low. The diagnosed probability distribution for the parameterized total eddy energy dissipation also seems to have a low bias, compared to the diagnosed dissipation of eddy kinetic energy in Pearson and Fox-Kemper (2018) from a high resolution ocean global circulation model. The resulting circulation metrics from utilizing  $\lambda^{-1}(\phi, \theta)$  inferred here, such as the total and thermal wind component of the Antarctic Circumpolar Current, is on the high side (at around 160 Sv, cf. Table 2 of Farneti et al., 2015), which is in line with the dynamical arguments provided by D. P. Marshall et al. (2017) that a higher eddy energy dissipation rate (so a shorter eddy energy dissipation time-scale) leads to increased Antarctic Circumpolar Current transport and steepening of isopycnals. Together, there is evidence in support of the inferred  $\lambda^{-1}(\phi, \theta)$  leading to an improved eddy energy signature in prognostic calculations, as well as being a physically plausible lower bound for the eddy energy dissipation time-scale.

Beyond providing a leading order constraint and estimate for eddy energy dissipation time-scale  $\lambda^{-1}(\phi, \theta)$  as progress towards understanding ocean energetic pathways, this work also highlights and demonstrates some perhaps lesser known but really quite powerful machinery relating to inverse methods and calculations, such as automatic code generation software such as Firedrake (Rathgeber et al., 2017), automatic adjoint generation libraries (e.g. Farrell et al., 2013; Maddison et al., 2019) and mesh generating software (Avdvis et al., 2018) that is expected to have applications in various branches of earth system modeling. Such tools have been applied to problems in global tidal modeling with uncertain bathymetry (David et al., 2019), uncertainty quantification associated with ice sheets Kolziol et al. (2021), Tsunami source inversion (Wallwork, 2021), and sediment transport modeling (Clare et al., 2022), to name a few examples.

In order to obtain the present lower bound for  $\lambda^{-1}(\phi, \theta)$ , some approximations were made in order to make the problem tractable. The approximations we made were (1) prescribing the stratification and thus removing dynamical feedbacks, and (2) the choice and assumption of data, cost functional, control variable and/or constraining model. As argued in the methodology section, the choice of prescribing the stratification, while reducing the complexity of the inference problem (e.g. removing coupling to an ocean global circulation model), has the consequence that the dynamical feedbacks are removed. As a consequence, the reduction in the complexity, we are somewhat restricted to the choice of target data, in this case to the total eddy energy signature as the state variable. Given the reduced amount of target data, it means we are somewhat limited to the choice and number of control variables we can take unless we impose severe and somewhat ad hoc regularizations.

Ultimately, those were choices we made in light of our primary objective, to provide a leading order reference constraint for which further investigations can be based on. A “simple” fix in principle is to dispense with prescribing the stratification parameters, and carry out a dynamically constrained inference calculation, which was part of



the motivation behind the present work. The related machinery is already in place in the form of the ECCO framework within MITgcm (e.g. Forget et al., 2015; Fukumori et al., 2018), set up utilizing the inbuilt algorithmic differentiation capabilities (e.g. Giering & Kaminski, 1998) to deriving adjoints for performing state estimation using the variational or smoothing approach (e.g. Kalnay, 2002). There is already a form of GEOMETRIC in MITgcm (from Mak et al., 2018), and the principal modification that would be required for the intended dynamical inference is to couple the GEOMETRIC parameterization for  $\kappa_{\text{gm}}$  accordingly to the existing ECCO framework, and including  $\lambda^{-1}(\phi, \theta)$  and possibly  $\alpha$  as additional control variables. By increasing the complexity of the problem, we are now also able to utilize ocean observational data as the target instead of just relying on the eddy energy signature. Given the large amounts of degrees of freedom associated with the proposed control variables, the adjoint method, which has a linear scaling in the complexity and requires a smaller amount of model calculations (one forward and one backward for each iteration; Kalnay, 2002; Gunzburger, 2003), is a particularly well-suited computational method (cf. Green’s function methods, while linear in complexity, requires ocean general circulation model runs scaling with the number of degrees of freedom, and is better when the number of control variables are low; e.g. Nguyen et al., 2011). While “simple” in principle, in practice the above proposal is still a formidable technical challenge and computationally expensive, and given there have been no strong constraints on  $\lambda^{-1}(\phi, \theta)$  thus far, the present result serves as an important leading order prior for the proposed dynamical inference calculation. The proposed work is currently underway and will be reported in a future publication.

A simpler procedure we have also considered is to stick with the strategy in this work, but diagnose the *time-varying* stratification and eddy energy data from a high resolution model, and consider an adjoint-based calculation where the cost functional is taken to be the mismatch between the parameterized eddy energy and target eddy energy over time. The inference will still not be dynamically constrained in the sense that the dynamical parameters for the proposed calculation will not be functions of the state variable, i.e. changes in  $\lambda^{-1}(\phi, \theta)$  and thus  $\hat{E}$  will have no bearing on the evolution of the stratification, given the latter is prescribed. While the calculation is certainly possible with the existing machinery since there are adjoint libraries that can be coupled to Firedrake (e.g. Farrell et al., 2013; Maddison et al., 2019), we are of the opinion that there is very little to be gained from that approach, given the theoretical and probably practical limitation is still that of prescribed stratification.

To close, we note that the variational methods considered here can be interpreted in the Bayesian as a maximum likelihood approach (e.g. Kalnay, 2002; Bui-Thanh et al., 2013), which by itself does not provide estimates of the uncertainties, and can have issues with over-tuning in cases where multiple different parameters are tuned at the same time (Williamson et al., 2017). Being able to quantify uncertainties associated with inference calculations will also be a research focus in the planned investigations. As an aside, sample prognostic calculations varying the Southern Ocean wind stress (cf. Mak et al., 2022) employing the spatially varying eddy energy dissipation time-scale appear to reproduce the eddy saturation phenomenon in the Antarctic Circumpolar Current transport in the thermal wind component (e.g., Munday et al., 2013; Farneti et al., 2015), and shows hints of eddy compensation (e.g. Gent & Danabasoglu, 2011; Viebahn & Eden, 2012; Bishop et al., 2016), although limitation in available computational resources in this case did not allow us to explore the sensitivity aspect fully. It is also of note that the change in the magnitude of the eddy energy dissipation time-scale in prognostic calculations, though relatively modest from a raw magnitude point of view, has a rather large effect on the resulting ocean state (see Table 2). In that sense, the results here reinforce the conclusions of Mak et al. (2022) that the ocean circulation displays a significant sensitivity to the eddy energy dissipation time-scale, even on the centennial time-scales. A thorough investigation into the sensitivity and

benefits afforded by a more complex representation of the eddy energetics in prognostic calculations (e.g., with the Ocean Model Intercomparison Project (OMIP) protocol; Griffies et al., 2016) is beyond the scope of the present work, but is ongoing and will be reported in due course.

## Data Availability

For the pre-processing, NEMO ORCA0083-N01 data was obtained from <http://gws-access.jasmin.ac.uk/public/nemo/>, provided by UK National Oceanography Center through the JASMIN service. The base version of CDFTOOLS was taken from <https://github.com/meom-group/CDFTOOLS>. For the optimization calculations, this work uses a natively installed version of Firedrake, with a mesh generated via the Qmesh package (<https://www.qmesh.org/>) via a Docker image, with the Firedrake wrapper of `tlm_adjoint` ([https://github.com/jrmaddison/tlm\\_adjoint](https://github.com/jrmaddison/tlm_adjoint)). The post-processing analysis uses standard Python packages. Modifications of CDFTOOLS, the relevant Python scripts, the processed data from this work (in both the native HDF5 finite element format as well as the various gridded versions), and documentation of software, versions and its dependencies are available on <http://dx.doi.org/10.5281/zenodo.6559892>.

## Acknowledgments

This research was funded by both the RGC Early Career Scheme 2630020 and the Center for Ocean Research in Hong Kong and Macau, a joint research center between the Qingdao National Laboratory for Marine Science and Technology and Hong Kong University of Science and Technology. JM would additionally like to thank Xiaoming Zhai, James Maddison and David Marshall for various technical comments on the various iterations of the present work.

## References

- Adkins, J. F. (2013). The role of deep ocean circulation in setting glacial climates. *Paleoceanography*, *28*, 539–561. doi: 10.1002/palo.20046
- Avdis, A., Candy, A. S., Hill, J., Kramer, C. S., & Piggott, M. D. (2018). Efficient unstructured mesh generation for marine renewable energy applications. *Renewable Energy*, *116*, 842–856. doi: 10.1016/j.renene.2017.09.058
- Bachman, S. D. (2019). The GM+E closure: A framework for coupling backscatter with the Gent and McWilliams parameterization. *Ocean Modell.*, *136*, 85–106. doi: 10.1016/j.ocemod.2019.02.006
- Barkan, R., Winters, K. B., & McWilliams, J. C. (2017). Stimulated imbalance and the enhancement of eddy kinetic energy dissipation by internal waves. *J. Phys. Oceanogr.*, *47*, 181–198. doi: 10.1175/JPO-D-16-0117.1
- Bishop, S. P., Gent, P. R., Bryan, F. O., Thompson, A. F., Long, M. C., & Abernathy, R. P. (2016). Southern Ocean overturning compensation in an eddy-resolving climate simulation. *J. Phys. Oceanogr.*, *46*, 1575–1592. doi: 10.1175/JPO-D-15-0177.1
- Bopp, L., Resplandy, L., Untersee, A., Le Mezo, P., & Kageyama, M. (2017). Ocean (de)oxygenation from the Last Glacial Maximum to the twenty-first century: insights from Earth System models. *Phil. Trans. R. Soc. A*, *375*, 20160323. doi: 10.1098/rsta.2016.0323
- Bui-Thanh, T., Ghattas, O., Martin, J., & Stadler, G. (2013). A computational framework for infinite-dimensional Bayesian inverse problems. Part I: The linearized case, with application to global seismic inversion. *SIAM J. Sci. Comput.*, *35*, A2494–A2523. doi: 10.1137/12089586X

- Burke, A., Stewart, A. L., Adkins, J. F., Ferrari, R., Jansen, M. F., & Thompson, A. F. (2015). The glacial mid-depth radiocarbon bulge and its implications for the overturning circulation. *Paleoceanography*, *30*, 1021–1039. doi: 10.1002/2015PA002778
- Byrd, R. H., Lu, P., Nocedal, J., & Zhu, C. (1995). A limited memory algorithm for bound constrained optimization. *SIAM J. Sci. Comput.*, *16*, 1190–1208. doi: 10.1137/0916069
- Cessi, P. (2008). An energy-constrained parametrization of eddy buoyancy flux. *J. Phys. Oceanogr.*, *38*, 1807–1819. doi: 10.1175/2007JPO3812.1
- Chelton, D. B., Schlax, M. G., & Samelson, R. M. (2011). Global observations of nonlinear mesoscale eddies. *Prog. Oceanogr.*, *91*, 167–216. doi: 10.1016/j.pocean.2011.01.002
- Chouksey, M., Eden, C., & Brüggemann, N. (2018). Internal gravity wave emission in different dynamical regimes. *Geophys. Res. Lett.*, *48*, 1709–1730. doi: 10.1175/JPO-D-17-0158.1
- Clare, M. C. A., Wallwork, J. G., Kramer, S. C., Weller, H., Cotter, C. J., & Piggott, M. D. (2022). Multi-scale hydro-morphodynamic modelling using mesh movement methods. *GEM: Int. J. Geomath.*, *13*, 2. doi: 10.1007/s13137-021-00191-1
- Danabasoglu, G., Yeager, S. G., Bailey, D., Behrens, E., Bentsen, M., Bi, D., . . . Wang, Q. (2014). North Atlantic simulations in Coordinated Ocean-ice Reference Experiments phase II (CORE-II). Part I: Mean states. *Ocean Model.*, *73*, 76–107. doi: 10.1016/j.ocemod.2013.10.005
- David, T. W., Balbus, S., Avdis, A., & Farrell, P. E. (2019). Influence of the tides on the evolution of early tetrapods: numerical and statistical perspectives. In *Geophysical research abstracts* (p. EGU2019-12885). EGU General Assembly 2019.
- Durrant, D. R. (2010). *Numerical methods for fluid dynamics* (2nd ed.). Springer.
- Eden, C., Czeschel, L., & Olbers, D. (2014). Toward energetically consistent ocean models. *J. Phys. Oceanogr.*, *44*, 3160–3184. doi: 10.1016/JPO-D-13-0260.1
- Eden, C., & Greatbatch, R. J. (2008). Towards a mesoscale eddy closure. *Ocean Modell.*, *20*, 223–239. doi: 10.1016/j.ocemod.2007.09.002
- Evans, L. C. (1998). *Partial differential equations*. American Mathematical Society.
- Farneti, R., Downes, S. M., Griffies, S. M., Marsland, S. J., Behrens, E., Bentsen, M., . . . Yeager, S. G. (2015). An assessment of Antarctic Circumpolar Current and Southern Ocean meridional overturning circulation during 1958–2007 in a suite of interannual CORE-II simulations. *Ocean Modell.*, *94*, 84–120. doi: 10.1016/j.ocemod.2015.07.009
- Farrell, P. E., Ham, D. A., Funke, S. W., & Rognes, M. E. (2013). Automated derivation of the adjoint of high-level transient finite element programs. *SIAM J. Sci. Comput.*, *35*, C369–C393. doi: 10.1137/120873558
- Ferrari, R., Jansen, M. F., Adkins, J. F., Burke, A., Stewart, A. L., & Thompson, A. F. (2014). Antarctic sea ice control on ocean circulation in present and glacial climates. *Proc. Natl Acad. Sci. USA*, *111*(24), 8753–8758. doi: 10.1073/pnas.1323922111
- Ferrari, R., & Wunsch, C. (2009). Ocean circulation kinetic energy: reservoirs, sources, and sinks. *Annu. Rev. Fluid Mech.*, *41*, 253–282.
- Ferrari, R., & Wunsch, C. (2010). The distribution of eddy kinetic and potential energies in the global ocean. *Tellus*, *62A*, 92–108.
- Forget, G., Campin, J.-M., Heimbach, P., Hill, C. N., Ponte, R. M., & Wunsch, C. (2015). ECCO version 4: an integrated framework for non-linear inverse modeling and global ocean state estimation. *Geosci. Model Dev.*, *8*, 3071–3104. doi: 10.5194/gmd-8-3071-2015
- Fox-Kemper, B., Adcroft, A. J., Böning, C. W., Chassignet, E. P., Curchitser, E. N., Danabasoglu, G., . . . Yeager, S. G. (2019). Challenges and prospects in ocean

- circulation models. *Front. Mar. Sci.*, *6*, 65. doi: 10.3389/fmars.2019.00065
- Fukumori, I., Heimbach, P., Ponte, R. M., & Wunsch, C. (2018). A dynamically consistent, multivariable ocean climatology. *Bull. Am. Meteorol. Soc.*, *90*, 2107–2128. doi: 10.1175/BAMS-D-17-0213.1
- Galbraith, E., & de Lavergne, C. (2019). Response of a comprehensive climate model to a broad range of external forcings: relevant for deep ocean ventilation and the development of late Cenozoic ice ages. *Clim. Dyn.*, *52*, 623–679. doi: 10.1007/s00382-018-4157-8
- Gaspar, P., Grégoris, Y., & Lefevre, J. (1990). A simple eddy kinetic energy model for simulations of the oceanic vertical mixing: Tests at station papa and long-term upper ocean study site. *J. Geophys. Res.*, *95*, 16179–16193. doi: 10.1029/JC095iC09p16179
- Gent, P. R., & Danabasoglu, G. (2011). Response to increasing southern hemisphere winds in CCSM4. *J. Climate*, *24*, 4992–4998. doi: 10.1175/JCLI-D-10-05011.1
- Gent, P. R., & McWilliams, J. C. (1990). Isopycnal mixing in ocean circulation models. *J. Phys. Oceanogr.*, *20*, 150–155. doi: 10.1175/1520-0485(1990)020<0150:IMIOCM>2.0.CO;2
- Gent, P. R., Willebrand, J., McDougall, T. J., & McWilliams, J. C. (1995). Parameterizing eddy-induced tracer transports in ocean circulation models. *J. Phys. Oceanogr.*, *25*, 463–474. doi: 10.1175/1520-0485(1995)025<0463:PEITTI>2.0.CO;2
- Giering, R., & Kaminski, T. (1998). Recipes for adjoint code construction. *ACM Trans. Math. Softw.*, *24*(4), 437–474. doi: 10.1145/293686.293695
- Gill, A. E. (1982). *Atmospheric-Ocean Dynamics*. Academic Press.
- Griffies, S. M. (1998). The Gent–McWilliams skew flux. *J. Phys. Oceanogr.*, *28*, 831–841. doi: 10.1175/1520-0485(1998)028<0831:TGMSF>2.0.CO;2
- Griffies, S. M., Danabasoglu, G., Durack, P. J., Adcroft, A. J., Bala, V., Böning, C. W., ... Yeager, S. G. (2016). OMIP contribution to CMIP6: experimental and diagnostic protocol for the physical component of the Ocean Model Intercomparison Project. *Geosci. Model Dev.*, *9*(9), 3231–3296. doi: 10.5194/gmd-9-3231-2016
- Grooms, I., Loose, N., Abernathey, R., Steinberg, J. M., Bachman, S. D., Marques, G., ... Yankovsky, E. (2021). Diffusion-based smoothers for spatial filtering of gridded geophysical data. *J. Adv. Model. Earth Syst.*, *13*, e2021MS002552. doi: 10.1029/2021MS002552
- Gunzburger, M. D. (2003). *Perspectives in flow control and optimization*. SIAM.
- Hewitt, H. T., Bell, M. J., Chassignet, E. P., Czaja, A., Ferreira, D., Griffies, S. M., ... Roberts, M. J. (2017). Will high-resolution global ocean models benefit coupled predictions on short-range to climate timescales? *Ocean Modell.*, *120*, 120–136. doi: 10.1016/j.ocemod.2017.11.002
- Jansen, M. F. (2017). Glacial ocean circulation and stratification explained by reduced atmospheric temperature. *Proc. Natl Acad. Sci. USA*, *114*(1), 45–50. doi: 10.1073/pnas.1610438113
- Jansen, M. F., Adcroft, A., Khani, S., & Kong, H. (2019). Toward an energetically consistent, resolution aware parameterization of ocean mesoscale eddies. *J. Adv. Model. Earth Syst.*, *1*, 1–17. doi: 10.1029/2019MS001750
- Jansen, M. F., & Held, I. M. (2014). Parameterizing subgrid-scale eddy effects using energetically consistent backscatter. *Ocean Modell.*, *80*, 36–48. doi: 10.1016/j.ocemod.2014.06.002
- Kalnay, E. (2002). *Atmospheric Modeling, Data Assimilation and Predictability* (Vol. 142). Cambridge University Press. doi: 10.1017/CBO9780511802270
- Klocker, A., & Marshall, D. P. (2014). Advection of baroclinic eddies by depth mean flow. *Geophys. Res. Lett.*, *41*, L060001. doi: 10.1002/2014GL060001
- Klymak, J. (2018). Non-propagating form drag and turbulence due to stratified flow

- over large-scale abyssal hill topography. *J. Phys. Oceanogr.*, *48*, 2383–2395. doi: 10.1175/JPO-D-17-0225.1
- Klymak, J., Balwada, D., Naveira Garabato, A. C., & Abernathey, R. (2021). Parameterizing nonpropagating form drag over rough bathymetry. *J. Phys. Oceanogr.*, *51*, 1489–1501. doi: 10.1175/JPO-D-20-0112.1
- Kolziol, C. P., Todd, J. A., Golberg, D. N., & Maddison, J. R. (2021). Fencics\_ice 1.0: A framework for quantifying initialization uncertainty for time-dependent ice sheet models. *Geosci. Model Dev.*, *14*, 5843–5861. doi: 10.5194/gmd-14-5843-2021
- Large, W. G., & Yeager, S. (2009). The global climatology of an interannually varying air-sea flux data set. *Clim. Dynam.*, *33*, 341–364. doi: 10.1007/s00382-008-0441-3
- Lin, X., Zhai, X., Wang, Z., & Munday, D. R. (2018). Mean, variability, and trend of Southern Ocean wind stress: Role of wind fluctuations. *J. Climate*, *31*, 3557–3573. doi: 10.1175/JCLI-D-17-0481.1
- Locarnini, R. A., Mishonov, A. V., Antonov, J. I., Boyer, T. P., Garcia, H. E., Baranova, O. K., . . . Seidov, D. (2013). World Ocean Atlas 2013, Volume 1: Temperature. In S. Levitus (Ed.), *Noaa atlas nesdis 73* (pp. 1–40).
- Maddison, J. R., Goldberg, D. N., & Goddard, B. D. (2019). Automated calculation of higher order partial differential equation constrained derivative information. *SIAM J. Sci. Comput.*, *41*, C417–C445. doi: 10.1137/18M1209465
- Maddison, J. R., & Marshall, D. P. (2013). The Eliassen–Palm flux tensor. *J. Fluid Mech.*, *729*, 69–102. doi: 10.1017/jfm.2013.259
- Madec, G. (2008). NEMO ocean engine. *Note du Pôle de modélisation, Institut Pierre-Simon Laplace (IPSL), No. 27*.
- Madec, G., & Imbard, M. (1996). A global ocean mesh to overcome the North Pole singularity. *Clim. Dyn.*, *12*, 381–388. doi: 10.1007/BF00211684
- Mak, J., Maddison, J. R., Marshall, D. P., & Munday, D. R. (2018). Implementation of a geometrically informed and energetically constrained mesoscale eddy parameterization in an ocean circulation model. *J. Phys. Oceanogr.*, *48*, 2363–2382. doi: 10.1175/JPO-D-18-0017.1
- Mak, J., Marshall, D. P., Madec, G., & Maddison, J. R. (2022). Acute sensitivity of global ocean circulation and heat content to eddy energy dissipation time-scale. *Geophys. Res. Lett.*, *49*(8), e2021GL097259. doi: 10.1029/2021GL097259
- Marshall, D. P., & Adcroft, A. J. (2010). Parameterization of ocean eddies: Potential vorticity mixing, energetics and Arnold’s first stability theorem. *Ocean Modell.*, *32*, 1571–1578. doi: 10.1016/j.ocemod.2010.02.001
- Marshall, D. P., Ambaum, M. H. P., Maddison, J. R., Munday, D. R., & Novak, L. (2017). Eddy saturation and frictional control of the Antarctic Circumpolar Current. *Geophys. Res. Lett.*, *44*, 286–292. doi: 10.1002/2016GL071702
- Marshall, D. P., & Johnson, H. L. (2017). Relative strength of the Antarctic Circumpolar Current and Atlantic Meridional Overturning Circulation. *Tellus A*, *69*, 1338884. doi: 10.1080/16000870.2017.1338884
- Marshall, D. P., Maddison, J. R., & Berloff, P. S. (2012). A framework for parameterizing eddy potential vorticity fluxes. *J. Phys. Oceanogr.*, *42*, 539–557. doi: 10.1175/JPO-D-11-048.1
- Marshall, J., Adcroft, A., Hill, C., Perelman, L., & Heisey, C. (1997). A finite volume, incompressible Navier–Stokes model for studies of the ocean on parallel computers. *J. Geophys. Res.*, *102*, 5753–5766. doi: 10.1029/96JC02775
- Marshall, J., Hill, C., Perelman, L., & Adcroft, A. (1997). Hydrostatic, quasi-hydrostatic, and non-hydrostatic ocean modelling. *J. Geophys. Res.*, *102*, 5733–5752. doi: 10.1029/96JC02776
- McDougall, T. J., & Jackett, D. R. (2005). The material derivative of neutral density. *J. Mar. Res.*, *63*(1), 159–185. doi: 10.1357/0022240053693734



- Melet, A., Hallberg, R., Adcroft, A., Nikurashin, M., & Legg, S. (2015). Energy flux into internal lee waves: Sensitivity to future climate changes using linear theory and a climate model. *J. Climate*, *28*, 2365–2384. doi: 10.1175/JCLI-D-14-00432.1
- Melet, A., Hallberg, R., Legg, S., & Nikurashin, M. (2014). Sensitivity of the ocean state to lee wave-driven mixing. *J. Phys. Oceanogr.*, *44*, 900–921. doi: 10.1175/JPO-D-13-072.1
- Molemaker, M. J., McWilliams, J. C., & Yavneh, I. (2005). Baroclinic instability and loss of balance. *J. Phys. Oceanogr.*, *35*, 1505–1517. doi: 10.1175/JPO2770.1
- Munday, D. R., Johnson, H. L., & Marshall, D. P. (2013). Eddy saturation of equilibrated circumpolar currents. *J. Phys. Oceanogr.*, *43*, 507–532. doi: 10.1175/JPO-D-12-095.1
- Nguyen, A. T., Menemenlis, D., & Kwok, R. (2011). Arctic ice-ocean simulation with optimized model parameters: Approach and assessment. *J. Geophys. Res.*, *116*, C04025. doi: 10.1029/2010JC006573
- Nielsen, S. B., Jochum, M., Eden, C., & Nuterman, R. (2018). An energetically consistent vertical mixing parameterization in CCSM4. *Ocean Modell.*, *127*, 46–54. doi: 10.1016/j.ocemod.2018.03.002
- Nikurashin, M., & Ferrari, R. (2011). Global energy conversion rate from geostrophic flows into internal lee waves in the deep ocean. *Geophys. Res. Lett.*, *38*, L08610. doi: 10.1029/2011GL046576
- Nikurashin, M., Vallis, G. K., & Adcroft, A. (2013). Routes to energy dissipation for geostrophic flows in the Southern Ocean. *Nature Geosci.*, *6*, L08610. doi: 10.1038/NGEO1657
- Nurser, A. J. G., & Bacon, S. (2014). The Rossby radius in the Arctic Ocean. *Ocean Sci.*, *10*, 967–975. doi: 10.5194/os-10-967-2014
- Olbers, D., & Eden, C. (2013). A global model for the diapycnal diffusivity induced by internal gravity waves. *J. Phys. Oceanogr.*, *43*, 1759–1779. doi: 10.1175/JPO-D-12-0207.1
- Pearson, B., & Fox-Kemper, B. (2018). Log-normal turbulence dissipation in global ocean models. *Phys. Rev. Lett.*, *120*, 094501. doi: 10.1103/PhysRevLett.120.094501
- Poulsen, M. B., Jochum, M., Maddison, J. R., Marshall, D. P., & Nuterman, R. (2019). A geometric interpretation of Southern Ocean eddy form stress. *J. Phys. Oceanogr.*, *49*, 2553–2570. doi: 10.1175/JPO-D-18-0220.1
- Rai, S., Hecht, M., Maltrud, M. E., & Aluie, H. (2021). Scale of oceanic eddy killing by wind from global satellite observations. *Sci. Adv.*, *7*, eabf4920. doi: 10.1126/sciadv.abf4920
- Rathgeber, F., Ham, D. A., Mitchell, L., Lange, M., Luporini, F., McRae, A. T. T., ... Kelly, P. H. J. (2017). Firedrake: Automating the finite element method by composing abstractions. *ACM Trans. Math. Softw.*, *43*(24), 1–27. doi: 10.1145/2998441
- Redi, M. H. (1982). Oceanic isopycnal mixing by coordinate rotation. *J. Phys. Oceanogr.*, *12*, 1154–1158. doi: 10.1175/1520-0485(1982)012<1154:OIMBCR>2.0.CO;2
- Rocha, C. B., Wagner, G. L., & Young, W. R. (2018). Stimulated generation: extraction of energy from balanced flow by near-inertial waves. *J. Fluid Mech.*, *847*, 417–451. doi: 10.1017/jfm.2018.308
- Roquet, F., Madec, G., McDougall, T. J., & Barker, P. M. (2015). Accurate polynomial expressions for the density and specific volume of seawater using the TEOS-10 standard. *Ocean Modell.*, *90*, 29–43. doi: 10.1016/j.ocemod.2015.04.002
- Rousset, C., Vancoppenolle, M., Madec, G., Fichefet, T., Flavoni, S., Barthélemy, A., ... Vivier, F. (2015). The Louvain-La-Neuve sea ice model LIM3.6:



- global and regional capabilities. *Geosci. Model Dev.*, *8*, 2991–3005. doi: 10.5194/gmd-8-2991-2015
- Salmon, R. (1980). Baroclinic instability and geostrophic turbulence. *Geophys. Astrophys. Fluid Dyn.*, *15*, 167–211.
- Sen, A., Scott, R. B., & Arbic, B. K. (2008). Global energy dissipation rate of deep-ocean low-frequency flows by quadratic bottom boundary layer drag: Computations from current-meter data. *Geophys. Res. Lett.*, *35*, L09606. doi: 10.1029/2008GL033407
- Takano, Y., Ito, T., & Deutsch, C. (2018). Projected centennial oxygen trends and their attribution to distinct ocean climate forcings. *Global Biogeochem. Cycles*, *32*, 1329–1349. doi: 10.1029/2018GB005939
- Viebahn, J., & Eden, C. (2012). Standing eddies in the Meridional Overturning Circulation. *J. Phys. Oceanogr.*, *42*, 1496–1508. doi: 10.1175/JPO-D-11-087.1
- Wallwork, J. G. (2021). *Mesh adaptation and adjoint methods for finite element coastal ocean modelling* (Doctoral dissertation, Imperial College London). doi: 10.25560/92820
- Williamson, D. B., Blaker, A. T., & Sinha, B. (2017). Tuning without over-tuning: parametric uncertainty quantification for the NEMO ocean model. *Geosci. Model Dev.*, *10*, 1789–1816. doi: 10.5194/gmd-10-1789-2017
- Wunsch, C. (1996). *The Ocean Circulation Inverse Problem*. Cambridge University Press. doi: 10.1017/CBO9780511629570
- Xu, C., Zhai, X., & Shang, X.-D. (2016). Work done by atmospheric winds on mesoscale ocean eddies. *Geophys. Res. Lett.*, *43*, 12174–12180. doi: 10.1002/2016GL071275
- Yang, L., Nikurashin, M., Hogg, A. M., & Sloyan, B. M. (2018). Energy loss from transient eddies due to lee wave generation in the Southern Ocean. *J. Phys. Oceanogr.*, *48*, 2867–2885. doi: 10.1175/JPO-D-18-0077.1
- Yang, L., Nikurashin, M., Hogg, A. M., & Sloyan, B. M. (2021). The impact of lee waves on the Southern Ocean circulation. *J. Phys. Oceanogr.*, *??*, ??–?? doi: 10.1175/JPO-D-20-0263.1
- Yang, Z., Zhai, X., Marshall, D. P., & Wang, G. (2021). An idealized model study of eddy energetics in the Western Boundary “Graveyard”. *J. Phys. Oceanogr.*, *51*, 1265–1282. doi: 10.1175/JPO-D-19-0301.1
- Zhai, X., Johnson, H. L., & Marshall, D. P. (2010). Significant sink of ocean-eddy energy near western boundaries. *Nature Geosci.*, *3*, 608–612. doi: 10.1038/NNGEO0943
- Zhai, X., Johnson, H. L., Marshall, D. P., & Wunsch, C. (2012). On the wind power input to the ocean general circulation. *J. Phys. Oceanogr.*, *42*, 1357–1365. doi: 10.1175/JPO-D-12-09.1
- Zhang, Y., & Vallis, G. K. (2013). Ocean heat uptake in eddying and non-eddying ocean circulation models in a warming climate. *J. Phys. Oceanogr.*, *43*, 2211–2229. doi: 10.1175/JPO-D-12-078.1
- Zweng, M. M., Reagan, J. R., Antonov, J. I., Locarnini, R. A., Mishonov, A. V., Boyer, T., . . . Biddle, M. M. (2013). World Ocean Atlas 2013, Volume 2: Salinity. In S. Levitus (Ed.), *Noaa atlas nesdis 74* (pp. 1–39).